Passive Sediment Augmentation (PSA) –

Phase I: Feasibility Study, Modeling, and Assessment

Waquoit Bay (Falmouth and Mashpee), Massachusetts

Prepared for:

WSP
100 Summer Street (13th Floor)
Boston, Massachusetts 02110

Massachusetts Office of Coastal Zone Management
100 Cambridge St., 9TH Floor
Boston, MA 02114

Waquoit Bay National Estuarine Research Reserve
131 Waquoit Hwy
East Falmouth, MA 02536

Prepared by:

Sustainable Coastal Solutions, Inc.
107A County Road
North Falmouth, Massachusetts 02556

W. Rockwell Geyer, Consultant
David K Ralston, Consultant

October 2024

Suggested citation:

Massachusetts Office of Coastal Zone Management [CZM 2024]. Passive Sediment Augmentation (PSA) – Phase I: Feasibility Study, Modeling, and Assessment Waquoit Bay (Falmouth and Mashpee), Massachusetts. Prepared by WSP, Sustainable Coastal Solutions, Inc., and Geyer & Ralston Consulting in partnership with the Waquoit Bay National Estuarine Research Reserve. 59 pgs.

This project has been financed with by the Massachusetts Office of Coastal Zone Management (CZM) with state funds and federal funds from National Oceanic and Atmospheric Administration (NOAA) award no. NA22nos4190075. The contents do not necessarily reflect the views and policies of the Executive Office of Energy and Environmental Affairs, NOAA, and CZM, nor does the mention of trade names or commercial products constitute endorsement or recommendation for use.

TABLE OF CONTENTS

LIST OF FIGURES

Figure **Page**

LIST OF TABLES

Table **Page**

1.0 Introduction

The Massachusetts Office of Coastal Zone Management (CZM) undertook this project to understand the feasibility of Passive Sediment Augmentation (PSA) as a sediment conservation and salt marsh preservation strategy in Massachusetts. The *Passive Sediment Augmentation* (PSA) modeling approach was geared toward understanding site-specific sediment transport in the Waquoit Bay system and providing results and conclusions that may be used to inform potential nearshore placement of dredged material for salt marsh nourishment at the modeled site(s). Based on the project requirements, the level of effort consisted of a thorough review of available data, an assessment of data gaps, a field deployment aimed at providing more detailed information regarding storm-induced currents and suspended sediment concentrations, and numerical sediment transport model simulations of dredged material placement options. The overall goal of the project was to improve the understanding of sediment transport mechanisms related to potential migration of dredged sediments placed adjacent to a marsh system onto the marsh plain, thereby enhancing long-term marsh plain accretion.

The project commenced with a review of the literature and analysis of existing data, mainly focused on the Waquoit Bay National Estuarine Research Reserve (WBNERR) timeseries data set from the long-term moorings. An observational field campaign was subsequently conducted in Waquoit Bay to address project-specific data needs. Time series measurements were made in the vicinity of potential sites for nearshore sediment placement to characterize the waves, currents, and suspended sediment concentrations under normal and storm conditions. To capture a range of characteristic storm and tidal forcing conditions, two potential nearshore placement sites with adjacent salt marsh were evaluated. Additionally, bed sediment was collected broadly in Waquoit Bay for grain size analysis to characterize the spatial variability in sediment composition and to inform the setup of the sediment transport modeling.

The model development was divided into several phases. In the first phase, an unstructured model grid was modified to focus grid resolution in the regions of interest near the mooring locations. This included resolving smaller tidal channels connecting the main part of Waquoit Bay to the sub-embayments, extending the grid into the intertidal marsh regions and modifying the friction parameter to account for the marsh vegetation. Updated model calibration was performed for hydrodynamics and no sediment to test the new grid against previously collected observations from February 2002 (Howes, et al. 2011). The previous Waquoit model by Sustainable Coastal Solutions had a similar spatial extent and demonstrated high model skill for water levels at multiple locations around the estuary.

The second phase of the model development added sediment transport and compared the results with the observations made in the 2023 field observations of this study. Model inputs were based on data collected from the observational study and other sources, and the verification process included comparison with the water level, velocity, wave, and turbidity time series. Simulation of select time intervals from the observations that represent a range of tidal and wave-forcing conditions were evaluated. These simulations provided a direct comparison of the model-predicted sediment concentrations and the data collected at the observation sites.

Model simulations were developed to represent the nearshore placement of dredged sediment at locations in consultation with CZM. As expected, sediment transport between

the subtidal estuary and the marsh occurred primarily during storm events when waves stresses increase sediment resuspension and storm surge increases water levels such that marshes are inundated for periods of hours to days. Simulations of storm events were conducted for both easterly and southerly events. Each of the storm simulations was evaluated for several factors to characterize the hydrodynamic and sediment transport conditions. The modeling team assessed how the different scenarios redistribute sediment from the simulated placements. The distribution of new sediment at the end of each simulation is likely to depend on wind direction, water level setup (regionally and locally withing the estuary), and sediment settling velocity. The model results are represented in maps and spatially aggregated calculations, e.g., how much of the sediment placement material deposited in the marsh regions.

2.0 Background and Review of Existing Data

Waquoit Bay is a coastal pond on the South Coast of Cape Cod, located in the glacial outwash plain from the most recent glaciation (Orson and Howes,1992; Figure 2.1). Its primary connection to Nantucket Sound is a narrow inlet, stabilized by jetties. It has an area of 3.7 km^2 and a typical depth of 1-2 m. Whereas the outwash plain is composed mostly of sand (Maio et al., 2016), the sediments within Waquoit Bay and its subestuaries is made up of a mixture of mud and sand, with finer sediments at depths greater than 1 m, and sand in the shallower water around the perimeter as well as in the more energetic tidal channels (Maio et al., 2016). The input of fresh water is mostly from groundwater, and there are no significant fluvial inputs of sediment (Maio et al., 2016).

Tidal range averages 0.6 m (Aubrey et al. 1993), making it a microtidal regime, with weak tidal currents of roughly 5 cm/s, except in the tidal channels at the mouth and at junctions between Waquoit Bay and its subestuaries, where the tidal velocities reach 1 m/s (Maio et al., 2016). Away from these channels, the main mechanism of sediment resuspension is due to waves, which routinely resuspend fine sediment along the shoreline but only resuspend sediment in the deeper basins under storm conditions (Maio et al., 2016).

Several of the subestuaries of Waquoit Bay, notably Sage Lot Pond and Tim's Pond, have significant areas of back-barrier salt marsh. Because the tidal range is so limited, storm surge is an important process affecting inundation of the marshes, with amplitudes of up to 1 m during strong Northeasterlies and hurricanes (Maio et al., 2016). The soils of these marshes have a very high organic carbon content relative to the inorganic sediment, with bulk density of inorganic sediment of 0.06 g/cm^3, and typical grain size of 20 μm (medium silt).

The sediment accumulation rate in the main body of Waquoit Bay is approximately 3 mm/y, close to the rate of sea-level rise (Maio et al., 2014). The source of this sediment is presumably from the erosion of the sediment along the shoreface of Nantucket and Vineyard Sounds, which provides a mixture of sand and silt from glacial outwash deposits. The stresses are too low under all but hurricane conditions to transport sand in the deeper waters of Waquoit Bay, explaining the prevalence of mud, with occasional layers of sand associated with previous hurricanes (Maio et al. 2016).

Limited data is available on suspended sediment concentrations in the Waquoit Bay system. Crawford (2002) investigated the influence of small-boat operation on suspended sediment concentrations, observing peak concentrations of over 400 mg/l associated with boat wakes. However ambient concentrations were found to be in the range of 10 to 20 mg/l. The Waquoit Bay National Estuarine Research Reserve (WBNERR) has extensive optical backscatter timeseries data at three sites in the Waquoit Bay system. These data indicate

sediment resuspension events associated with storms, with readings of up to 40 ntu (https://cdmo.baruch.sc.edu/). However, the suspended sediment concentrations (sediment mass per volume) were not measured in association with these turbidity measurements.

Figure 2.1 Aerial image of the Waquoit Bay system (source Google, 2021)

3.0 Data Gaps

An important question related to the feasibility of Passive Sediment Augmentation is to determine the potential for sediment resuspension and transport in regions adjacent to the coastal ponds with back-barrier marshes. Based on the previous data, the most likely source of sediment resuspension is the contribution of locally generated storm waves in the shoals along the edge of the bay, where the sediment type transitions from mud to sand. Measurements of waves and currents as well as suspended sediment concentration in these regions would be required over a period that includes significant storm conditions. In addition, more detailed information about the grain size distribution of sediment in different parts of Waquoit Bay is required to determine the ambient sediment resuspension conditions.

4.0 Field Program Description

4.1. Timeseries instruments

Observations were conducted from March 10 to May 9, 2023 in Waquoit Bay. Timeseries instruments were deployed outside and inside the mouths of Tim's Pond and Sage Lot Pond (Figure 4.1). At the outer sites (roughly 1-m water depth), upward-looking Aquadopp acoustic Doppler current profilers were deployed on low-profile "T" frames to provide measurements of currents and acoustic backscatter at 10-cm intervals through the water column, sampling at 5-minute intervals. Temperature, salinity, pressure and optical backscatter were measured at 0.4 m above the bottom at all of the sites with RBR Concerto instruments, sampling at 1-minute intervals. Waves were measured with high frequency (4 Hz) sampling of pressure in the outer sampling sites, with the sensors fixed just below the minimum depth of the water surface (roughly 0.6 m above the bottom). See Appendix C for a description of the methodology for determining tsignificant wave height.

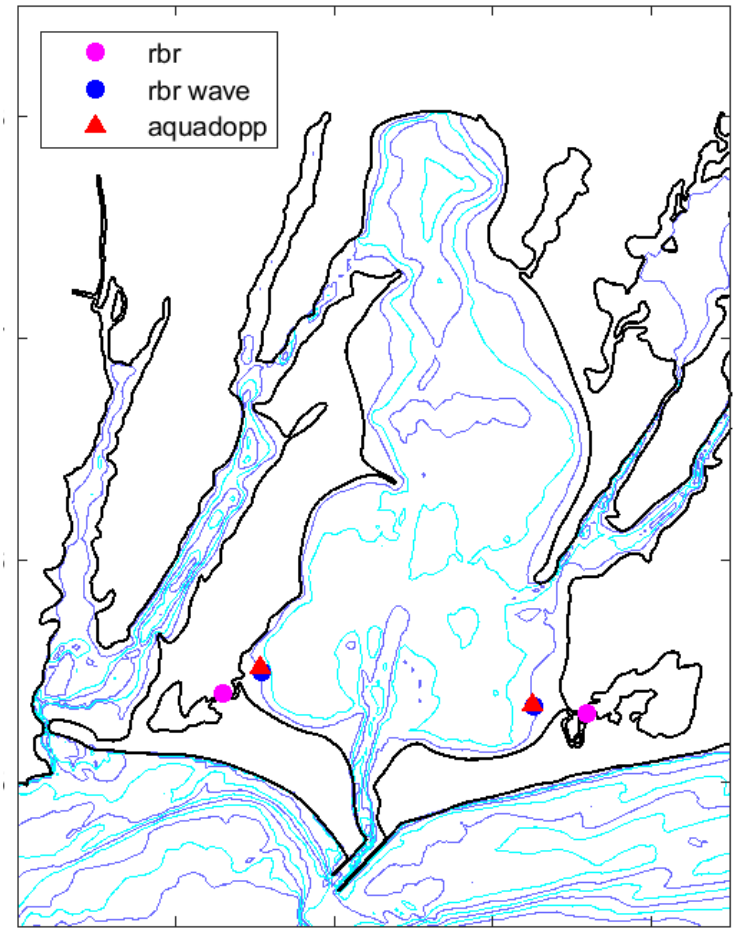

Figure 4.1. Locations of the timeseries instruments adjacent to Tim's Pond and Sage Lot Pond. Bathymetry contour interval is 1-m. Bathymetry is based on the 2018 USACE survey for the East Coast.

4.2. Sediment Sampling

Grab samples were obtained at 22 stations throughout Waquoit Bay and in Sage Lot Pond and Tim's Pond on May 3, 2023. A Ponar grab sampler was used to get surficial sediment, roughly the top 5-10 cm of the sea-bed. The grain size of the samples was analyzed with a Malvern laser diffraction particle sizer at the Woods Hole Oceanographic Institution sedimentology lab.

4.3. Suspended Sediment Calibration

The storm conditions in which significant sediment was resuspended were not conducive to field work, so laboratory calibration of the optical backscatter sensors was performed in the laboratory following the field study. Suspensions were generated using one of the sediment samples with grain-size typical of the Waquoit Bay mud samples, across a range of concentrations between 200 and 600 mg/l. Although these concentrations were expected to exceed the observed field

concentrations, the nearly linear response of the OBS over concentrations in the tested range and lower provides adequate calibration for the observed concentrations. Unfortunately, the optical backscatter sensor data from the field deployment were generally too noisy to be of use in quantifying the suspended sediment concentrations, probably due to fouling as well as detritus emanating from the marshes. However, the acoustic backscatter from the aquadopp current profilers were not influenced by this fouling, and they provided an alternative means of measuring the suspended sediment. Appendix A describes how the acoustic backscatter was calibrated, based on comparison with a limited time period in which one of the optical backscatter sensors provided useful data.

5.0 Field Program Results

5.1. Timeseries data

5.1.1. Water Level: Tides and Storm Surge

One of the important factors influencing the delivery of sediment to the marsh face is the variability of water level due to tides and storm surge. The pressure sensors at the four mooring sites (Figure 5.1) indicate that tidal fluctuations and longer timescale fluctuations due to meteorological forcing caused comparable variations in water level. Typical tidal range was roughly 0.6 m, and storm surge added another 0.6 m of variability, as indicated by the thick black line that represents the water level with the tides filtered out. The differences in water level between different stations was found to be only several cm.

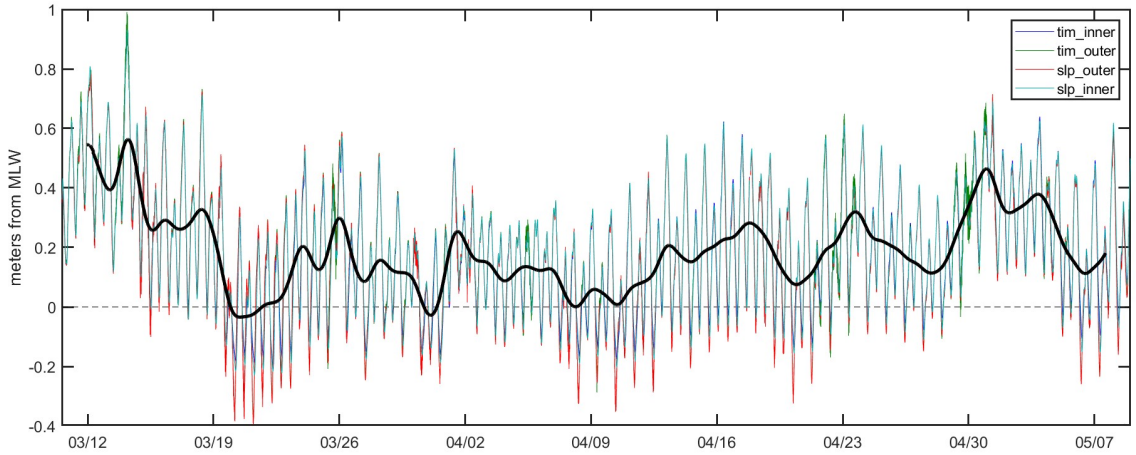

Figure 5.1 Water level at the four measurement locations during the observation period from March to May, 2023. The thin colored lines show the unfiltered water level, corrected to mean low water (MLW), and the thick line is the tidally filtered water level based on the average of the four stations.

Comparison of the low frequency water level fluctuations at Waquoit Bay to the NOAA gauges at Woods Hole and Boston (Figure 5.2) indicates that most of the low-frequency variability (e.g., storm surge) is regional, rather than local. The peaks in water level were found to be mainly associated with Easterly winds, as discussed in Section 5.1.3.

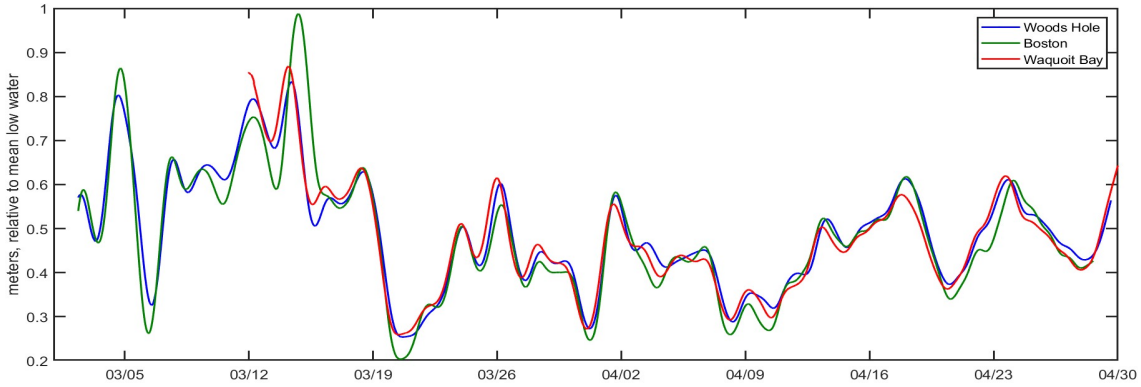

Figure 5.2 Comparison of low-frequency (storm surge) variations in water level at Woods Hole, Boston and Waquoit Bay for the measurement period.

5.1.2. Currents

Currents were measured at the outer sites at Tim's Pond and Sage Lot Pond. The vertically averaged currents are shown in Figure 5.3. At both locations, the maximum current was around 0.2 m/s, and typical currents were around 0.05 m/s. This is consistent with previous observations of the currents in Waquoit Bay (Maio et al., 2014). Interestingly, the direction of the maximum currents were in opposite directions at the two sites, directed away from the inlets, or in the ebb direction with respect to the inlets (Figure 5.4). In the case of Sage Lot Pond, the strong currents were correlated with the drop in water level, corresponding to the ebb tide during the larger of the two tides during each day (i.e., the diurnal tide). This was not the case at the Tim's Pond entrance. It did not show any evidence of tidal variability at its entrance. The pulses of strong current occurred over longer timescales, and they were apparently related to wind- or wave-forcing of the larger scale flow. The vertical structure of the current at Tim's Pond during one of the pulses is shown in Figure 5.5. The pulse lasts for approximately 12 hours, with maximum currents near the water surface reaching 0.35 m/s, and much weaker currents at depth. The mechanism causing this offshore jet was not determined in this study. Because the currents were weak at the bottom, it may not be relevant to the resuspension and transport of suspended sediment, except insofar as it represents a mechanism for dispersing waterborne material across Waquoit Bay.

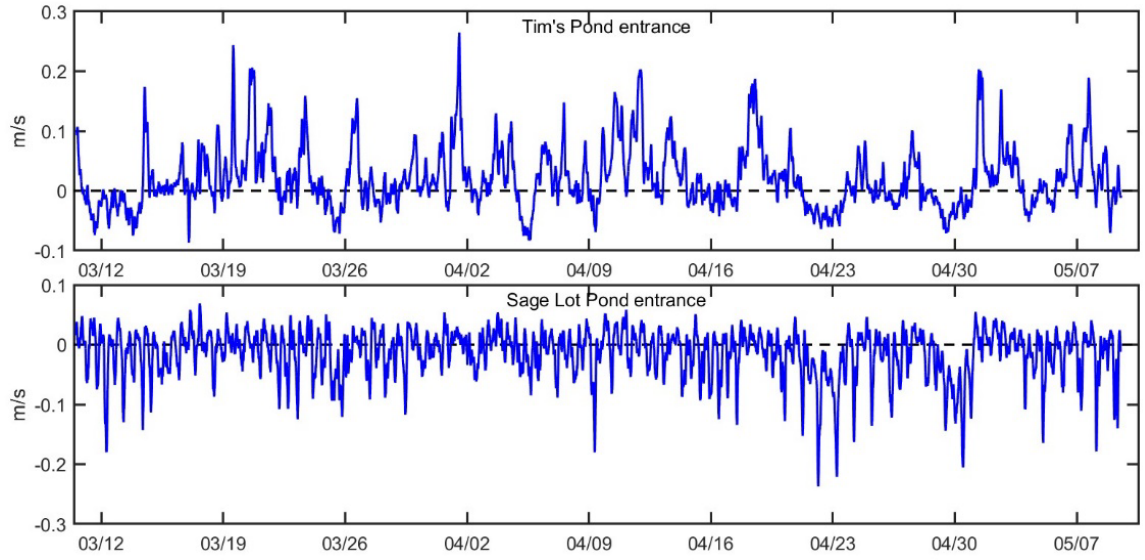

Figure 5.3 Vertically averaged currents at Outer Tim's Pond (upper panel) and Outer Sage Lot Pond (lower panel). Positive currents are in the eastward direction, and negative currents are in the westward direction. At both locations, the strongest currents are directed away from the inlets.

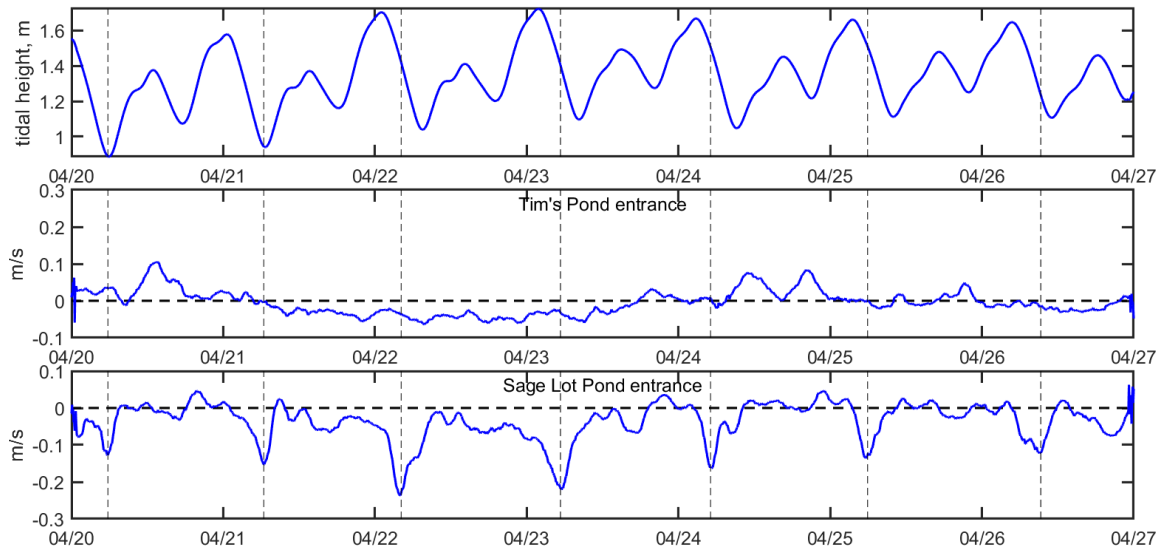

Figure 5.4 A one-week interval of tidal height (upper panel), currents at Tim's Pond (middle panel) and currents at Sage Lot Pond (lower panel). The pulses at Sage Lot Pond are aligned with the drop in water level, i.e., ebb conditions. No ebb pulses are evident at the Tim's Pond entrance.

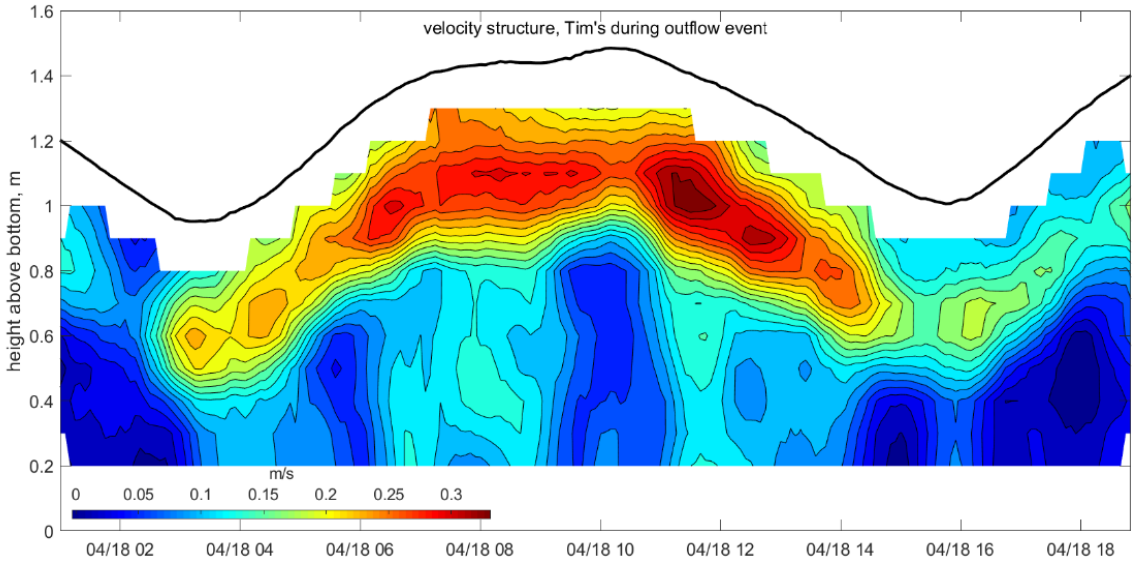

Figure 5.5 Contour plot of eastward currents at Tim's Pond entrance on April 18, 2023, corresponding to one of pulses.

5.1.3. Wind, Waves and suspended sediment

The time period of the field measurements includes a variety of wind events from different directions, indicated on the top panel of Figure 5.6. The strongest winds reached nearly 20 m/s—gale force. In spite of the large magnitude of the winds, the measured waves only reached a maximum height of 0.3 m. This is because the entrance to Waquoit Bay is so narrow that the larger waves from Nantucket Sound do not enter, so all of the waves are locally generated, and they are "fetch-limited", i.e. their size is determined by how large a distance the wind blows over before reaching the measurement location.

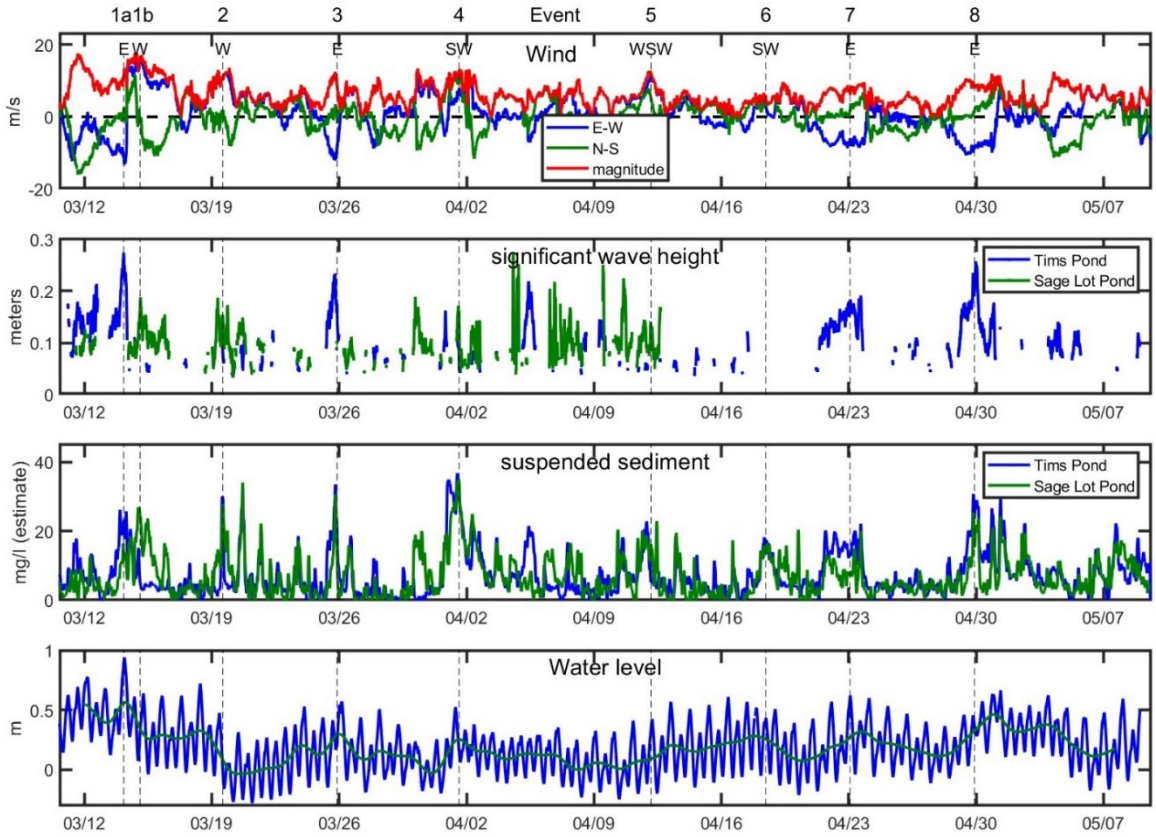

Figure 5.6 Timeseries of wind (top panel), wave height (2nd panel), suspended sediment concentration (3rd panel) and water level (bottom panel). The winds were measured at the Nantucket Sound NOAA buoy. The significant wave height was measured at the outer stations at the entrances of Tim's Pond and Sage Lot Pond. The wave sensor at Sage Lot Pond malfunctioned after 4/13. The suspended sediment concentration was based on the acoustic backscatter data from the aquadopps at the outer stations at each site. The water level is the average of the two outer sites, referenced to mean low water.

The suspended sediment concentration showed peaks generally corresponding to the times that the waves reached their maximum amplitude. Based on the calibration of the sensors, the peak concentrations were approximately 30 mg/l, although as discussed in Appendix B, the uncertainty of this estimate may be as much as a factor of two. Nevertheless, the time-series data clearly indicate that the waves were strongly correlated with the peaks in suspended sediment concentration.

Water level showed peaks during times of easterly events, due to storm surge. This is discussed in more detail in context with the evaluation of individual events.

5.1.4. Events

The vertical lines in Figure 5.6 correspond to eight "events" in which significant peaks in suspended sediment occurred at one or both of the timeseries locations in Waquoit Bay. Table 5.1 describes the wind, wave and water level conditions for each event. Events 1a, 3, 7 and 8 were Easterly wind events, and they all showed higher wave height and suspended sediment concentrations at Tim's Pond than Sage Lot Pond. This is explained by the fact that

Tim's Pond is on the downwind side of Waquoit Bay during Easterlies, resulting in larger fetch. The larger waves resulted in enhanced sediment resuspension at Tim's Pond. Easterlies also showed higher water levels. Events 1b, 2 and 5 were predominantly Westerlies, with higher waves and suspended sediment at Sage Lot Pond, consistent with the fetch dependence. Southwest wind events (4 and 6) showed relatively high suspended sediment concentrations at both sites, with relatively low wave height at Tim's Pond. This may be explained by sediment resuspension in Nantucket Sound, and tidal advection of the suspended sediment into Waquoit Bay.

Table 5.1 Suspended Sediment Events

Event	Date	Wind Speed (m/s)	Wind Direction	Water Level (m)	Tims Pond		Sage Lot Pond	
					Wave Ht (m)	Susp. Sed (mg/l)	Wave Ht (m)	Susp. Sed (mg/l)
1a	3/14	**17**	E	**.9**	**.27**	**22**	.10	10
1b	3/15	**17**	W	.5	.13	5	.17	**20**
2	3/19	12	W	.1	.06	5	**.20**	**20**
3	3/26	**18**	E	.5	**.23**	**33**	.10	**29**
4	4/2	13	SW	.5	.09	**35**	**.17**	**35**
5	4/12	12	WSW	.4	.06	6	.14	16
6	4/18	6	SW	.5	.07	**18**	-	**18**
7	4/22	8	E	**.6**	**.18**	**20**	-	15
8	4/30	10	E	**.6**	**.26**	**31**	-	**25**

Figure 5.7 shows a detailed comparison of the response to Events 1a and 1b, showing the contrast between Easterly forcing and Westerly forcing.

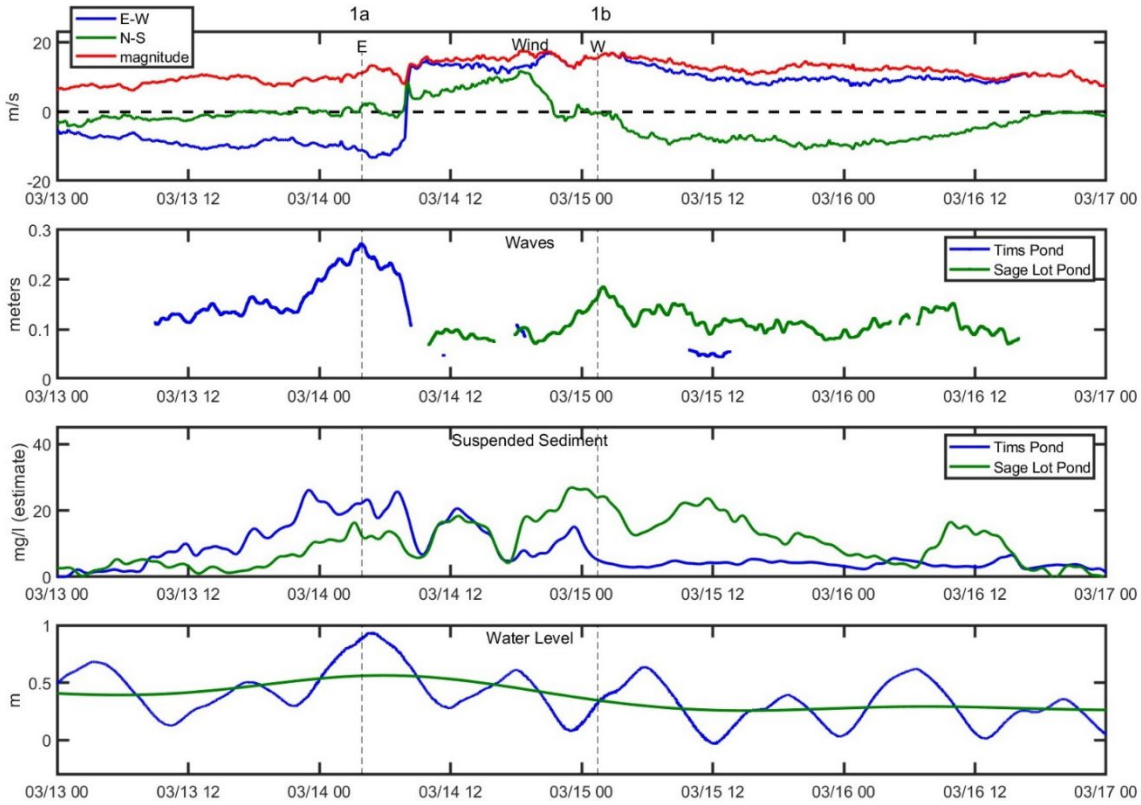

Figure 5.7 Timeseries of wind (top panel), wave height (2nd panel), suspended sediment concentration (3rd panel) and water level (bottom panel) for a 4-day period including Events 1a and 1b. The waves at Sage Lot Pond were too small to be resolved during Event 1a, whereas the waves at Tim's Pond (the downwind side of the Bay during the Easterly) were among the biggest observed during the deployment. During the Westerly event 1B, the waves were much bigger at Sage Lot Pond. The suspended sediment shows the same dependence on wind direction as the wave height, with stronger resuspension at Tim's Pond during the Easterly and stronger resuspension at Sage Lot during the westerly. Water level is much higher during the Easterly, due to the storm surge.

5.2. Grab Sample Data

Detailed results of the grain size analysis of the grab samples are shown in Appendix A. Figure 5.8 shows the spatial distribution of grain size as reported by fine fraction (1 being all mud, and 0 being all sand). The muddier samples (yellow and red) are all in the deeper water, and the sandier samples (blue shades) are in the shallow water near the shore or in tidal channels. One exception is the muddy station in the upper northwest corner of Waquoit Bay, where muddy sediment gets trapped near the shore, perhaps due to generally smaller waves in that part of the Bay. Figure 5.9 shows the grain size distribution, obtained by the laser diffraction particle sizer. The distribution is generally bimodal, with a sand peak and a coarse silt peak.

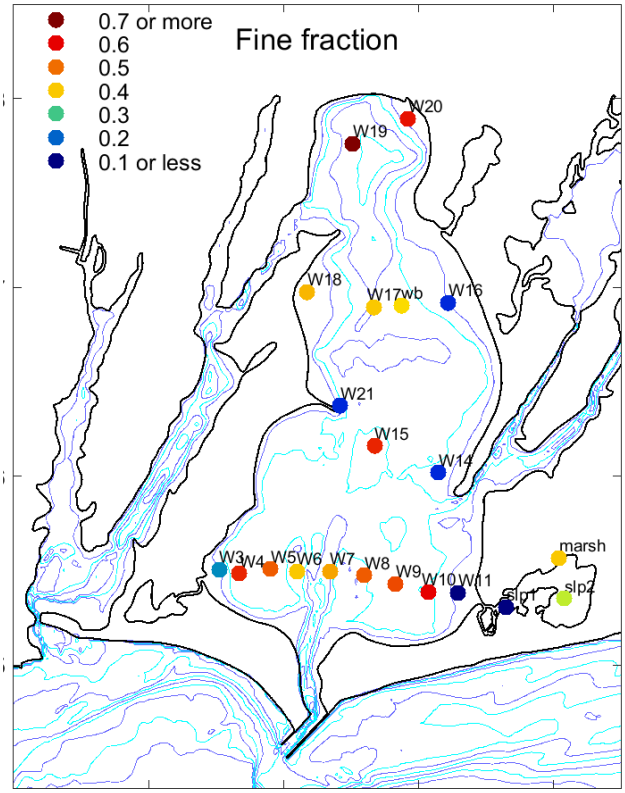

Figure 5.8 Fine fraction of sediment from grab samples (fraction less than 63 μm.).

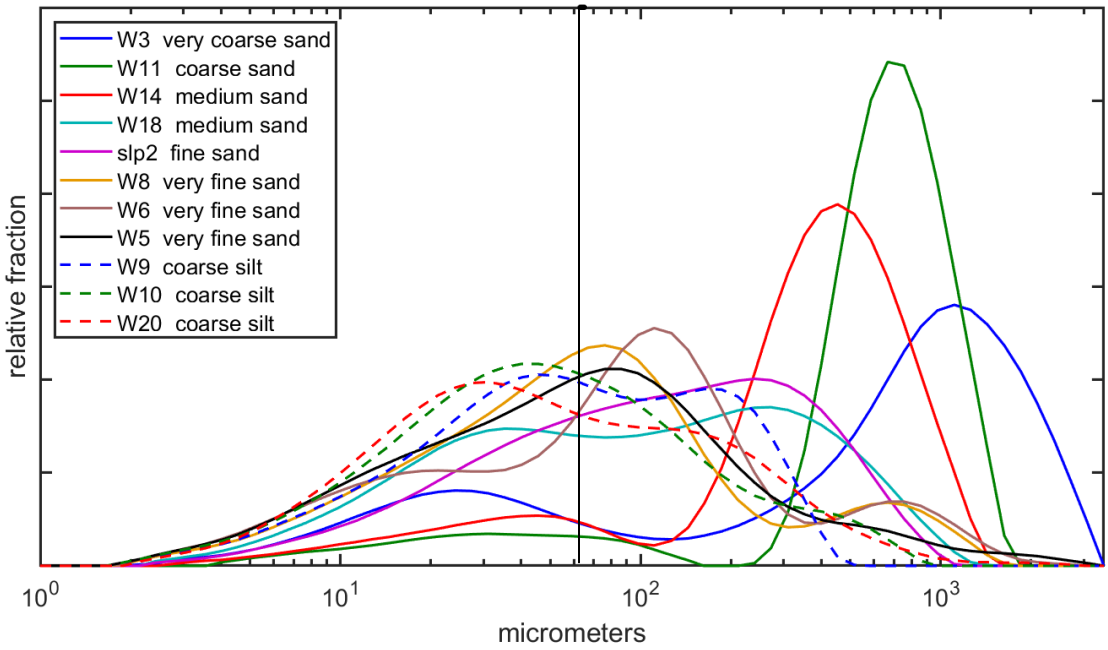

Figure 5.9 Grain size distribution of selected grab samples (see Appendix A for locations). The vertical line shows the boundary between mud and sand.

6.0 Delft3D Flow Model of Waquoit Bay (*Standalone Model*)

A hydrodynamic model of Waquoit Bay system was used to simulate accurate flow characteristics with Waquoit Bay to develop forcing conditions used in the sediment transport modeling of this project. For this, a previously developed hydrodynamic model of the Waquoit Bay system was expanded, calibrated, and corroborated using publicly available sources of data as well as data collected from previous studies. These data include tidal measurements, LiDAR, and bathymetric surveys.

6.1. Model Development

The model was implemented using Delft3D Flexible Mesh (FM) modeling suite, which includes the D-Flow FM hydrodynamic module. D-Flow FM is a flexible mesh, finite volume code that includes a morphologic model that simulate tidally driven sediment transport and morphology change. D-Flow FM is an advanced code that can solve three-dimensional hydrodynamics and sediment transport. The model utilizes a grid mesh that can be constructed using a variety of polygonal elements, with up to six sides. This allows for easy construction of model framework that conforms well to complex shorelines and sinuous channels and that can include high degrees of mesh resolution in areas only where it is desired. Sub-grid-scale flow modifying structures such as weirs and thin dams can be specified for the model runs. Combined with Delft3D Wave (D-Waves module), it can be implemented as a fully integrated wave, hydrodynamic, and morphological model.

The full extent of the complete hydrodynamic model grid is represented in Figure 6.1. The grid was developed to cover the entire Waquoit Bay system to ensure flow dependencies between Waquoit Bay and the Eel River estuary, via the Seapit River, are considered. The original grid domain was modified to include computational cells across the barrier beach system between Waquoit Bay and Nantucket Sound. The model incorporates tidal open boundaries offshore of the Eel River and Waquoit Bay inlets in Nantucket Sound. The offshore lateral boundaries are configured as Neumann gradient boundaries that allow the development of longshore currents in the offshore area of the grid.

Figure 6.1 Hydrodynamic model mesh of the Waquoit Bay system. The model domain includes all of the major subembayments within the system (Quashnet River was not included in this modeling effort), as well as the barrier beaches to the south that border the estuary and Nantucket Sound.

The flexible mesh grid was utilized to increase the spatial resolution in the nearshore areas of Tim's Pond and Sage Lot Pond. A close-up of the grid focused on inlets to Tim's Pond and Sage Lot Pond is shown in Figures 6.2 and Figure 6.3. Grid spacing ranges from a minimum grid cell length of roughly 5 meters in the vicinity of Tim's Pond and Sage Lot Pond to a maximum grid cell length of 70 meters at the offshore boundary in Nantucket Sound. Lower grid resolution was also applied to regions far away from the study area that are gradually sloped with relatively smooth shoreline geometry such as the northern extents of Waquoit Bay, where grid cell lengths were set to approximately 50 meters.

Figure 6.2 Closeup image of the hydrodynamic flexible mesh in the vicinity of the inlet to Sage Lot Pond. The grid coverage of the inlet area and primary marsh channel includes reduced grid spacing (approximately 5 meters) to increase the resolution and better represent the physical characteristics of area in the model.

Figure 6.3 Closeup image of the hydrodynamic flexible mesh in the vicinity of the inlet to Tim's Pond. The grid coverage of the inlet area and primary marsh channel includes reduced grid spacing (approximately 5 meters) to increase the resolution and better represent the physical characteristics of area in the model.

A composite bathymetry dataset, constructed using sources obtained from the National Ocean Service (NOS), was interpolated to the model mesh (NOS, 1998; Figure 6.4). This bathymetry dataset is primarily based on the 2018 LiDAR and 2021 LiDAR surveys. These data were used to refine and update the bathymetry in the areas of Tim's Pond and Sage Lot Pond to best represent the most current condition of the inlets and marsh channels within the ponds. The continuously updated New England coastal DEM produced by NOAA was used for the far-offshore region and small gaps not covered by the LiDAR surveys. Previously collected single beam fathometer bathymetry data were used to corroborate the LiDAR and DEM bottom elevations within the upper reaches of Childs River, Eel Rive, Seapit River, Hamblin Pond, and Great River.

The model was run using a variable time step that was determined based on the metrics of model stability (Courant number, based on velocity, water depth and grid cell size). The maximum model time step was at 30 seconds, but could be reduced at times when the Courant number calculated for grid cells exceeds the threshold value of 1.

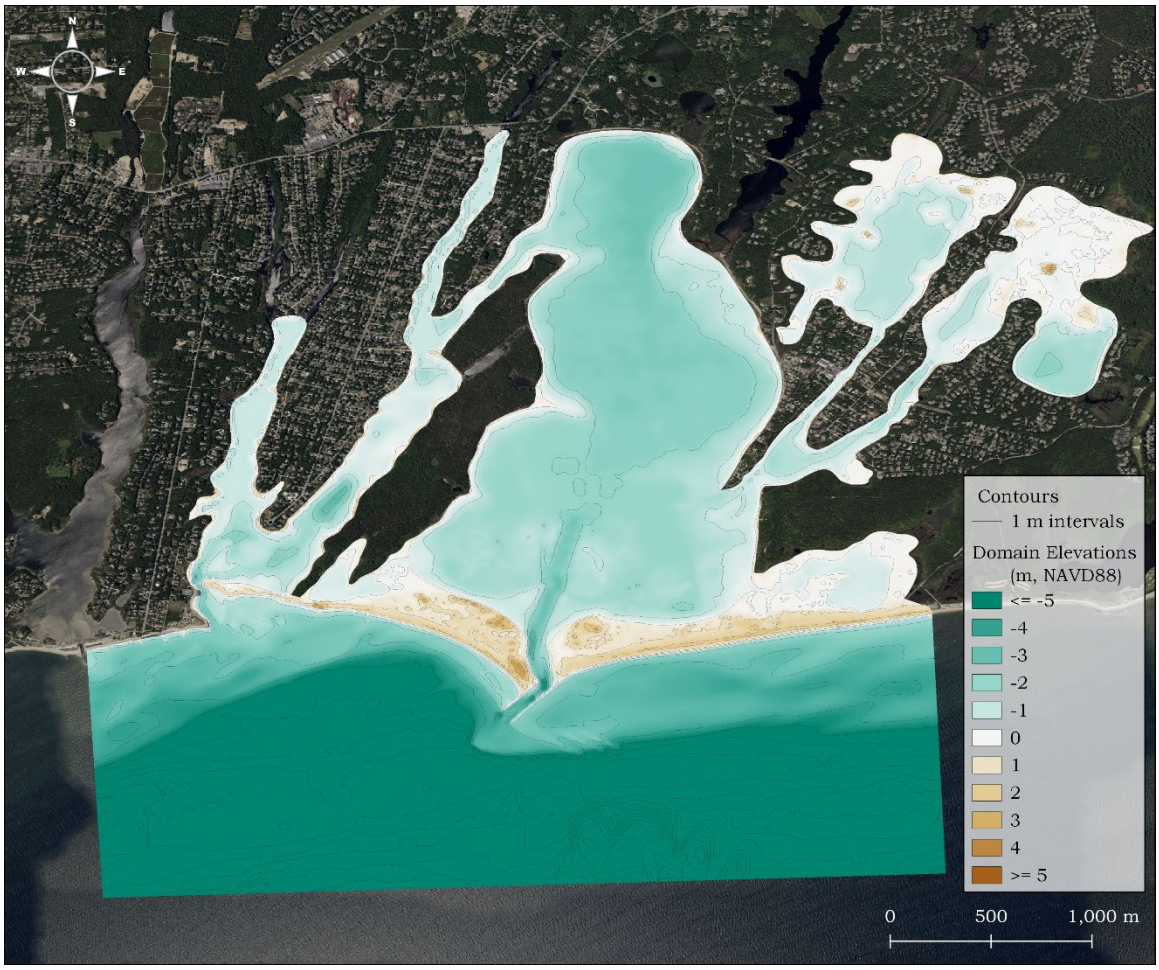

Figure 6.4 Topographic and bathymetric datasets of the Waquoit Bay system interpolated to model grid. The blue-green color palette displays elevations less than 0 meters (NAVD88), darkening as depth increases. Likewise, elevations greater than 0 meters (NAVD88) are represented using a palette of light brown to dark brown. Contours spaced at 1-meter vertical intervals are shown as gray lines.

6.2. Model Calibration

The newly gridded model of the Waquoit Bay system was calibrated using the time frame between January 18 and February 19, 2002, which includes the dates of the tide data collection period for the previously developed hydrodynamic model of Waquoit Bay. The calibration procedure ensures that the model accurately simulates the natural flow processes within the system by minimizing the variation of the hydrodynamic characteristics between the measured data and the model output. Numerous model simulations are typically required for an estuary model, specifying a range of friction and eddy viscosity coefficients, to calibrate the model.

6.2.1. Harmonic Analysis

The model was calibrated using tidal measurements within different regions of the embayment (Figure 6.5) to ensure that the model accurately simulates the natural hydrodynamics of the system. The six tide measuring stations are referred to by the region of the embayment system in which they were located: 1) offshore Eel River Inlet, 2) Eel River West, 3) Childs River, 4) Waquoit Bay, 5) Hamblin Pond, and 6) Great River. The gauges were deployed longer than the 29-day minimum required to record the monthly maximum and minimum astronomical tide ranges, and also to provide a record sufficient in duration to perform a harmonic analysis to determine the 23 main tidal constituents at each location. The elevation of each gauge was surveyed relative to NGVD29 and converted to NAVD88 using NOAA's VDatum. Data from the offshore record were used to develop the open boundary condition of the hydrodynamic model. Data from the other five locations were used to calibrate the model.

Figure 6.5 Locations of the six gauges used to collect the tidal measurements used to calibrate the hydrodynamic model.

The tides in the Waquoit Bay system are semi-diurnal, meaning that there are typically two complete tide cycles in a day. Plots of the tide data from the six gauges are shown in Figure 6.6, for approximately two 12.4-hour tide cycles, near the spring the tide maximum (full moon occurred January 28, 2002). This plot demonstrates the slight variation in the time and elevation of the high and low tides across the measurement stations. These phase (delay) differences provide potential for flow through the system, in addition to the potential supplied by the rise and fall of the tide offshore. The time lag of low tide measured at offshore gauge and the gauge located in Hamblin Pond (from Figure 6.6) is approximately 1 hour and 40 minutes.

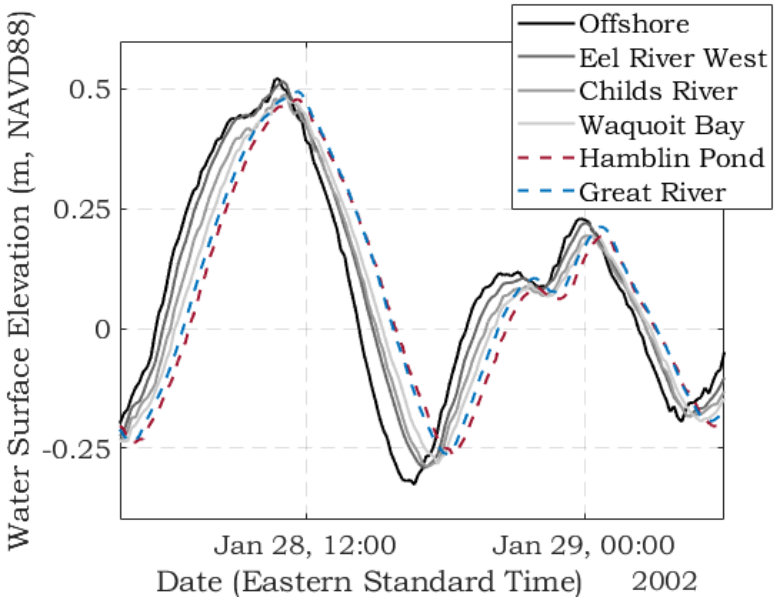

Figure 6.6 Two tide cycles at the six tide gauge locations in the Waquoit Bay system, illustrating the tidal phase and amplitude differences across the system.

Standard tide datums were computed from the tide records. These datums are presented in Table 6.1. For most NOAA tide stations, these datums are computed using 19 years of tide data, the definition of a tidal epoch. For this study, a significantly shorter time span of data was available, however, these datums still provide a useful comparison of the tidal dynamics within the system. The Mean Higher High Water (MHHW) and the Mean Lower Low Water (MLLW) levels represent the mean of the daily highest and lowest water levels, respectively. The Mean High Water (MHW) and Mean Low Water (MLW) levels represent the mean of all high and low tides of a record. The mean Tide Level (MTL) is simply the mean of MHW and MLW. The MTL, MLW, and MLLW levels at the Hamblin Pond and Waquoit Bay stations show that maximum attenuation of the tide occurs in the inner regions of the embayment system where tidal exchange is typically less efficient.

A harmonic analysis of the six tidal data sets was performed to produce the tidal amplitude and phase of the major constituents. This analysis also yielded quantitative assessment of the relative influence of non-tidal, or residual, processes (such as wind forcing) on the hydrodynamics of the system. Harmonic analysis is a mathematical procedure that fits sinusoidal functions of the known frequencies to the measured signal. The observed astronomical tide is therefore the sum of several individual tidal constituents, with a particular

amplitude and frequency. For demonstration purposes a graphical representation of tidal constituents added together is shown in Figure 6.7, where the observed tide is equal to the superposition of the various constituent curves shown. The amplitudes and phase of the 23 known tidal constituents result from this procedure. Table 6.2 presents the amplitudes of the eight most influential constituents at the six tide stations in the Waquoit Bay system.

Table 6.1 Tide datums computed from data records collected offshore of the Eel River inlet entrance channel and in the upper regions of Eel River West, Child's River, Waquoit Bay, Hamblin Pond, and Great River (January 18, 2002 to February 19, 2002). Datum elevations are given in meters relative to NAVD88.

Tide Datum	Offshore	Eel River West	Child's River	Waquoit Bay	Hamblin Pond	Great River
Maximum Tide	0.57	0.57	0.53	0.52	0.52	0.53
MHHW	0.35	0.35	0.34	0.33	0.32	0.33
MHW	0.24	0.23	0.23	0.22	0.22	0.23
MTL	-0.02	-0.02	-0.02	-0.02	-0.01	-0.02
MLW	-0.28	-0.27	-0.26	-0.25	-0.24	-0.26
MLLW	-0.35	-0.32	-0.32	-0.30	-0.28	-0.31
Minimum Tide	-0.57	-0.46	-0.54	-0.41	-0.44	-0.48

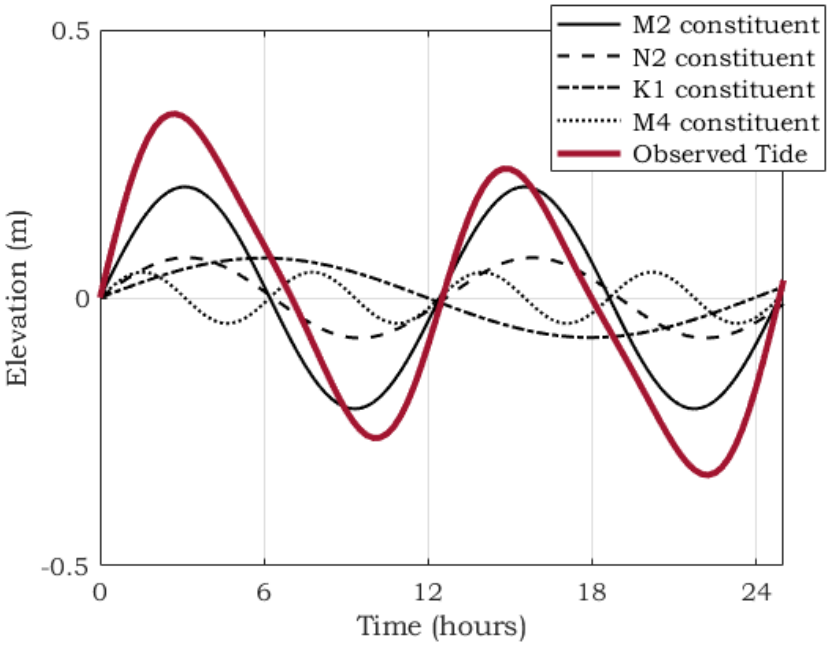

Figure 6.7 Example of an observed astronomical tide as the sum of its primary constituents.

Table 6.2 Major tidal constituents determined for gauge locations in the Waquoit Bay system (January 18, 2002 to February 19, 2002)

	Amplitude (m)							
Constituent	M_2	M_4	M_6	S_2	N_2	K_1	O_1	M_{sf}
Period (hours)	12.42	6.21	4.14	12.00	12.66	23.93	25.82	354.61
Offshore	0.21	0.05	0.02	0.02	0.08	0.07	0.07	0.01
Eel River West	0.20	0.04	0.02	0.02	0.07	0.08	0.07	0.01
Child's River	0.20	0.03	0.02	0.02	0.07	0.07	0.07	0.01
Waquoit Bay	0.20	0.03	0.01	0.02	0.07	0.07	0.07	0.01
Hamblin Pond	0.19	0.02	0.02	0.02	0.06	0.07	0.07	0.01
Great River	0.20	0.03	0.02	0.02	0.07	0.07	0.07	0.01

The M_2, or the familiar twice-a-day lunar semi-diurnal tide, is the strongest contributor to the signal with an offshore amplitude of 0.21 meters. The total range of the M_2 tide is twice the amplitude, or 0.42 meters. The M_4 and M_6 tides are higher frequency harmonics of the M_2 lunar tide (exactly half the period of the M_2 for the M_4, and one third of the M_2 period for the M_6), and result from frictional attenuation of the M_2 tide in shallow water. The other major tide constituents show little variation across the system. The S_2 is the largest solar constituent and is related to the gravitational forces of the Sun on the tides. Like the M_2, the S_2 (12.00-hour period) is a semi-diurnal tidal constituent; however, because the sun is much farther from the Earth the amplitude of the S_2 is usually much smaller than the M_2. The effects of the S_2 are most commonly seen in spring tides and neap tides, during which the Sun and Moon are either aligned or perpendicular, respectively, creating a beat phenomenon. The amplitude of the S_2 provides a relatively small contribution (0.02 m) to the tidal fluctuation and is consistent across all of the regions in the Waquoit Bay system. The M_{sf} is a lunarsolar fortnightly constituent with a period of approximately 14 days, and is the result of shallow water interactions occurring from the periodic conjunction of the sun and moon. The M_{sf} has an offshore amplitude of 0.01 meters. The other semi-diurnal tide, the N_2 (12.66-hour period) tide, contributes across the system to varying degrees offshore amplitudes of 0.08 meters. The variation of the N_2 is often related to the variation observed by the M_2 constituent because the N_2 is a result of the 27-day variation in the Moon's distance to the Earth. The diurnal tides (once daily), K_1 and O_1, both possess amplitudes of approximately 0.07 meters.

Along with the variation in constituent amplitudes throughout the system, the phase change of the tide is seen from the results of the harmonic analysis. Table 6.3 shows the delay of the M_2 at different points in the Waquoit Bay system, relative to the timing of the M_2 constituent offshore of the Eel River inlet entrance channel. The greatest delay is at the Hamblin Pond gauge station, which also showed the largest reduction of the M_2 amplitude (Table 6.2). Compared to other locations instrumented in this study, the Hamblin Pond station shows the greatest tidal attenuation compared to the tide offshore.

In addition to the harmonic analysis, the tide data were further evaluated to determine the importance of tidal versus non-tidal processes to changes in water surface elevation. These other processes include wind forcing (set-up or set-down) within the estuary, as well as sub-tidal oscillations of the sea surface (e.g., caused by large scale weather systems). Variations in

water surface elevation can also be affected by freshwater discharge into the system, if these volumes are relatively large compared to tidal flow.

Table 6.3 M_2 tidal constituent phase delay (relative to tides immediately offshore Eel River Inlet) for gauge locations in the Waquoit Bay system, determined from measured tide data.

Station	Delay (minutes)
Eel River West	23.4
Child's River	33.6
Waquoit Bay	46.7
Hamblin Pond	72.8
Great River	64.6

The results of the analysis to determine the energy distribution (or variance) of the original water elevation time series for the Waquoit Bay system is presented in Table 6.4, and is compared to the energy content of the astronomical tidal signal (recreated by summing the contributions from the 23 constituents determined from the harmonic analysis). Subtracting the tidal signal from the original elevation time series (measured data) resulted with the non-tidal, or residual, portion of the water elevation changes. The energy of this non-tidal signal is compared to the tidal signal, and yields a quantitative measure of how important these non-tidal physical processes can be to hydrodynamic circulation within the estuary. Figure 6.8 shows the comparison of the measured tide from outside Eel River Inlet, with the computed astronomical tide resulting from the harmonic analysis, and the subsequent non-tidal residual. Atmospheric contributions on the tides that may seem small in other areas of New England can influence rather large impacts in the Waquoit Bay system due to the relatively small tidal range in the vicinity of Eel River Inlet. The tidal residual is seen to be generally less than 1 foot throughout the deployment period; however, in many instances the magnitude of the residual tide is larger than the predicted tide.

Table 6.4 shows that there is a reduction in tidal energy in areas farther from the inlet. This is another indication of the tidal attenuation through the system. The analysis also shows that tidal processes are responsible for approximately 64% of the water level changes in the Waquoit Bay system. The remaining 36% was the result of atmospheric forcing, due to winds or barometric pressure gradients. The small contribution of the residual to the complete tide signal provides confidence that the system can be adequately modeled using tide data series.

Table 6.4 Percentages of Tidal versus Non-Tidal Energy for the Waquoit Bay system, January 18 to February 19, 2002

Tide Gauge Location	Total Variance ($m^2 \cdot sec$)	Tidal (%)	Non-tidal (%)
Offshore Eel River Inlet	0.047	64.5	35.5
Eel River West	0.045	63.5	36.5
Child's River	0.042	63.4	36.6
Waquoit Bay	0.041	63.5	36.5
Hamblin Pond	0.039	64.2	35.8
Great River	0.042	63.5	36.5

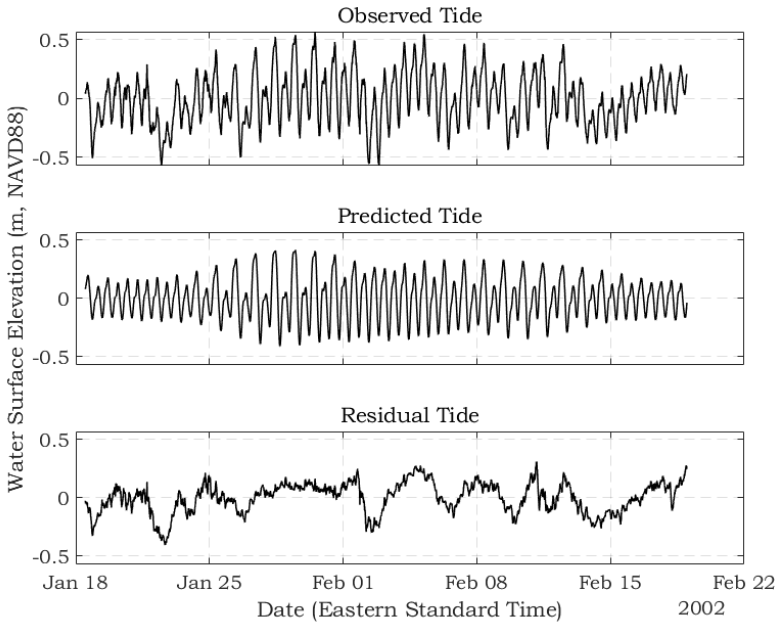

Figure 6.8 Plot showing the comparison between the measure tide time series (top), and the predicted astronomical tide (middle) computed using 23 individual tide constituents determined in the harmonic analysis of the Waquoit Bay system tide gauge measurements. The residual tide (bottom) is computed as the difference between the measured and predicted time series.

6.2.2. Model Output

Calibration of the hydrodynamic model required a close match between the modeled and measured tides in each of the embayment regions where the tides were measured. The comparison of modeled and measured tides is presented in Figure 6.9 and Figure 6.10, and in Table 6.5. Tide constituents for both modeled and measured tides were calculated to ensure proper phasing and amplitude of the tide across the embayment system. During the process of calibration, values of friction coefficients specified for the entire model domain were varied. For the Waquoit model, the Mannings formulation of friction was utilized, with applied Mannings coefficient values ranging from 0.025 to 0.04 applied to different areas of the grid. Generally, the calibration shows the considerable skill of the model with constituent errors

that are of the order of 10^{-2} meters, and phase errors that are less than (with the exception of Hamblin Pond and Great River) or equal to the magnitude of the time step associated with the measured tide data (10 minutes). The relatively large phase errors observed in Hamblin Pond and Great River were expected due to coarsely resolved grid spacing in Little River and the lack of consideration for supplemental flushing through the creek north of Seconsett Island. These errors were disregarded due to the negligible effects this region of the system would have on the hydrodynamics on Tim's Pond and Sage Lot Pond.

Table 6.5 Tidal constituents for measured water level data and calibrated model output, with model error amplitudes, for the Waquoit Bay system.

Measured Tide						
Location	Constituent Amplitude (m)				Phase (deg)	
	M_2	M_4	M_6	K_1	φM_2	φM_4
Offshore	0.21	0.05	0.02	0.07	82.40	-59.95
Eel River	0.20	0.04	0.02	0.08	93.72	-36.39
Childs River	0.20	0.04	0.02	0.07	98.62	-25.87
Waquoit Bay	0.19	0.03	0.01	0.07	104.95	-12.80
Hamblin Pond	0.19	0.02	0.01	0.07	117.57	22.14
Great River	0.20	0.03	0.02	0.07	113.59	11.01
Modeled Tide						
Location	Constituent Amplitude (m)				Phase (deg)	
	M_2	M_4	M_6	K_1	φM_2	φM_4
Offshore	0.21	0.05	0.02	0.07	82.75	-59.34
Eel River	0.20	0.04	0.02	0.07	92.25	-36.20
Childs River	0.19	0.03	0.02	0.07	101.51	-13.40
Waquoit Bay	0.19	0.03	0.02	0.07	104.53	-13.42
Hamblin Pond	0.12	0.00	0.01	0.06	155.34	-21.44
Great River	0.16	0.01	0.01	0.07	134.26	42.29
Error (measured - modeled)						
Location	Amplitude Error (m)				Phase Error (min.)	
	M_2	M_4	M_6	K_1	φM_2	φM_4
Offshore	0.00	0.00	0.00	0.00	-0.72	-0.64
Eel River	0.00	0.00	0.00	0.00	3.02	-0.19
Childs River	0.00	0.00	0.00	0.00	-5.98	-12.91
Waquoit Bay	0.01	0.00	0.00	0.00	0.86	0.64
Hamblin Pond	0.07	0.02	0.01	0.01	-78.19	45.12
Great River	0.04	0.02	0.00	0.01	-42.78	-32.38

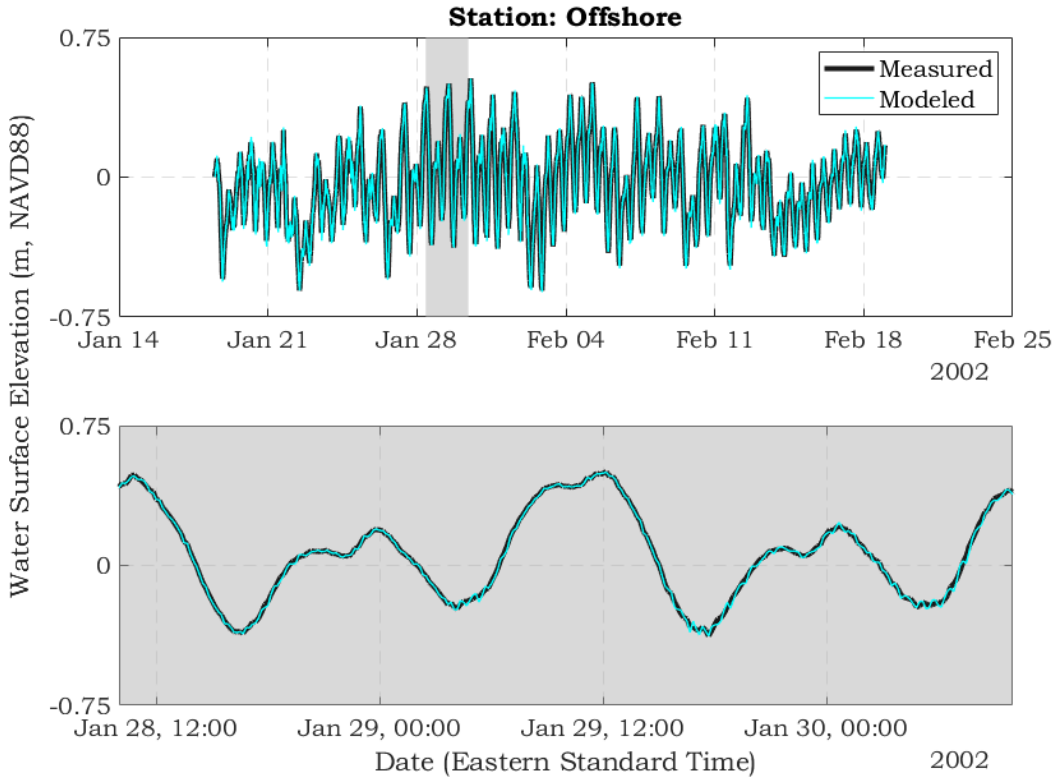

Figure 6.9 Comparison of measured and modeled tides at the offshore tide station for Waquoit Bay. The bottom plot represents a zoomed in view of the gray-shaded area from the top plot.

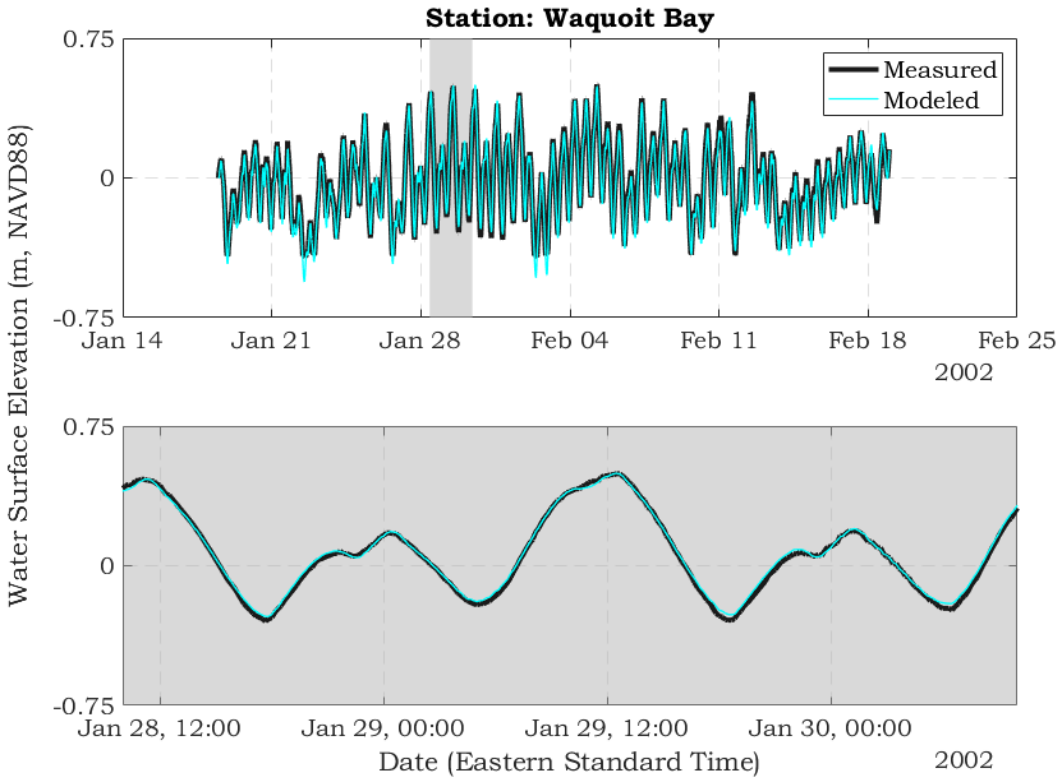

Figure 6.10 Comparison of measured and modeled tides at the Waquoit Bay tide station. The bottom plot represents a zoomed in view of the gray-shaded area from the top plot.

6.3. Flushing Characteristics of Waquoit Bay

Examples of model output at model time steps that correspond to maximum flood and ebb velocities in the areas of Tim's Pond and Sage Lot Pond are shown in Figures 6.11 through 6.14. These plots show the distribution of tidal flows through the inlets and channels within Tim's Pond and Sage Lot Pond generally differ between each pond during flood and ebb portions of the tide cycle. Generally, ebbing portions of the tide experience greater flow velocities in Sage Lot Pond, whereas flows in Tim's Pond reach a maximum velocity during the flooding portion of the tide. During flooding tides, peak flow velocities occur at the convergence of the channel network within the inner marsh before entering Tim's Pond, but flows entering Sage Lot Pond reach the greatest velocities within the inlet channel just behind the barrier spit. During ebbing tides (Figure 6.12 and Figure 6.14), peak flow velocities are more broadly distributed across the marsh region fronting Tim's Pond with smaller relative increases in velocities near the inlet and barrier spit, rather than the inner marsh. However, in Sage Lot Pond, peak flow velocities during ebbing tides occur in a similar location to those during flooding tides. Overall, tidal driven currents are larger in Sage Lot Pond than in Tim's Pond, with velocities reaching approximately 1.1 m/s and 0.5 m/s during ebb tides and 0.9 m/s and 0.6 m/s during flood tides, respectively.

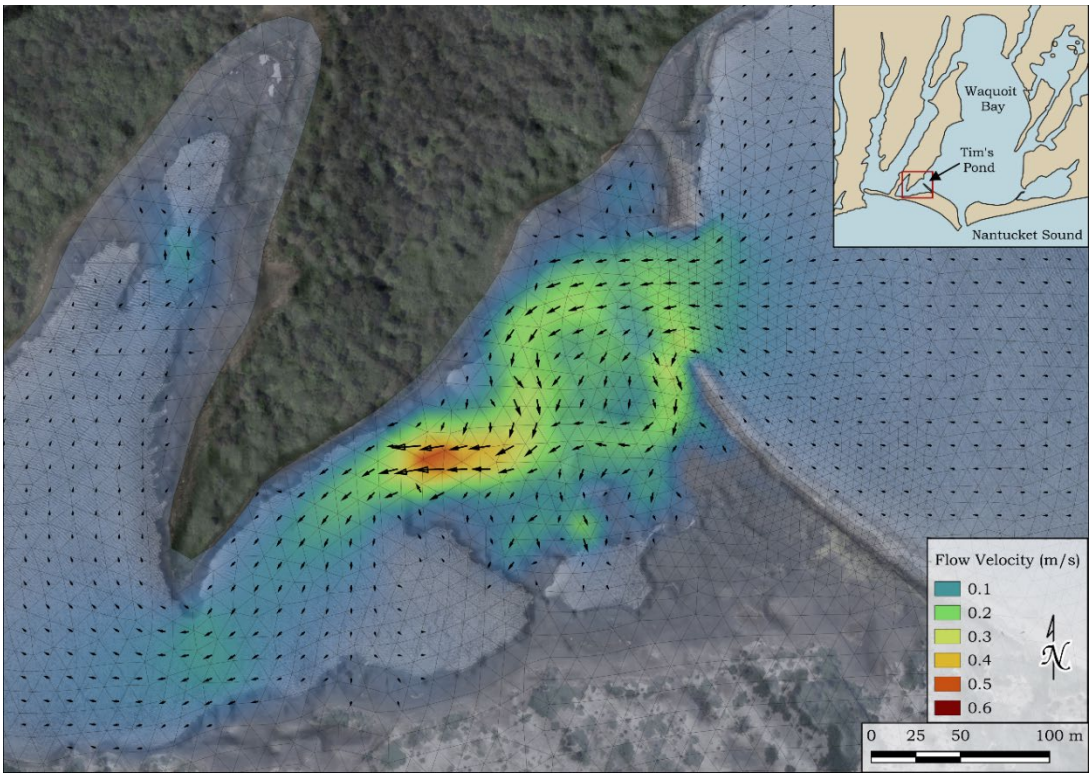

Figure 6.11 Example of model output during a time of maximum flood currents at Tim's Pond.

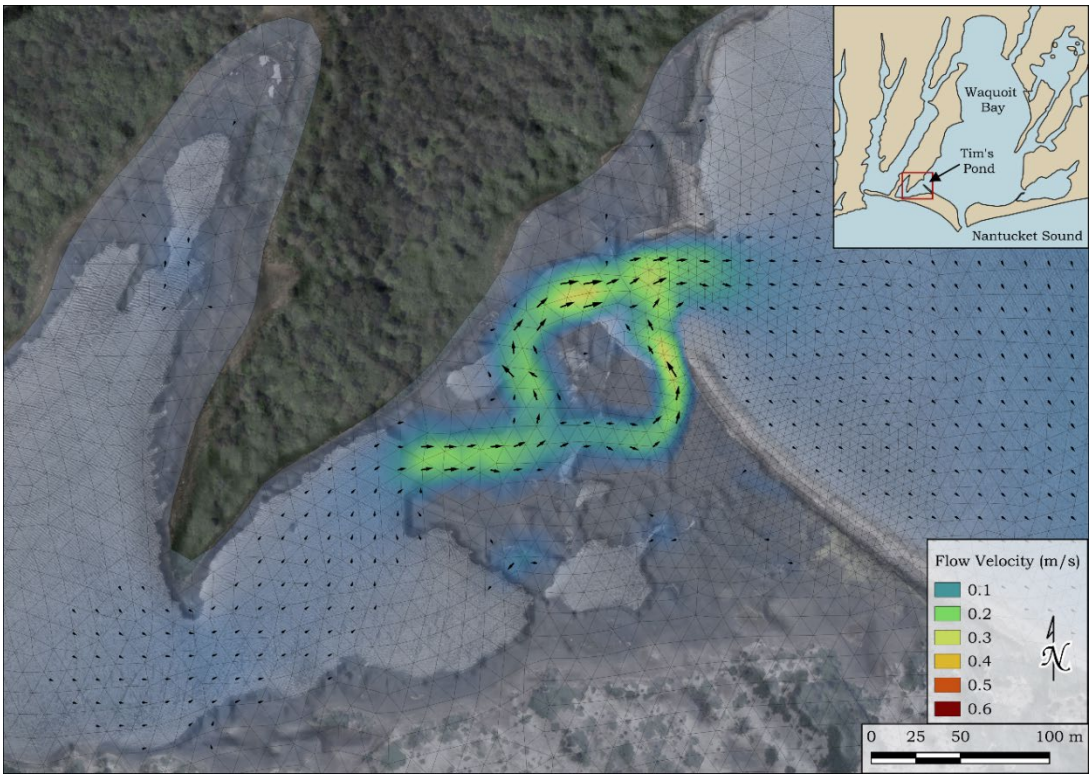

Figure 6.12 Example of model output during maximum ebb currents at Tim's Pond.

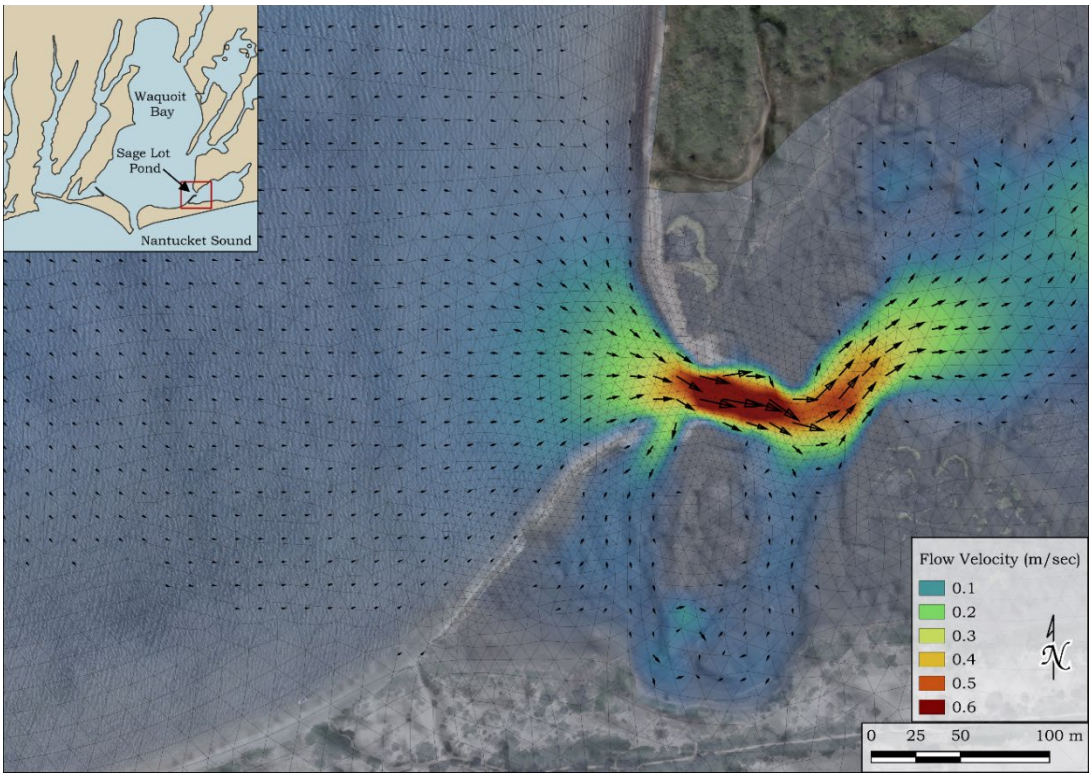

Figure 6.13 Example of model output during maximum flood currents at Sage Lot Pond.

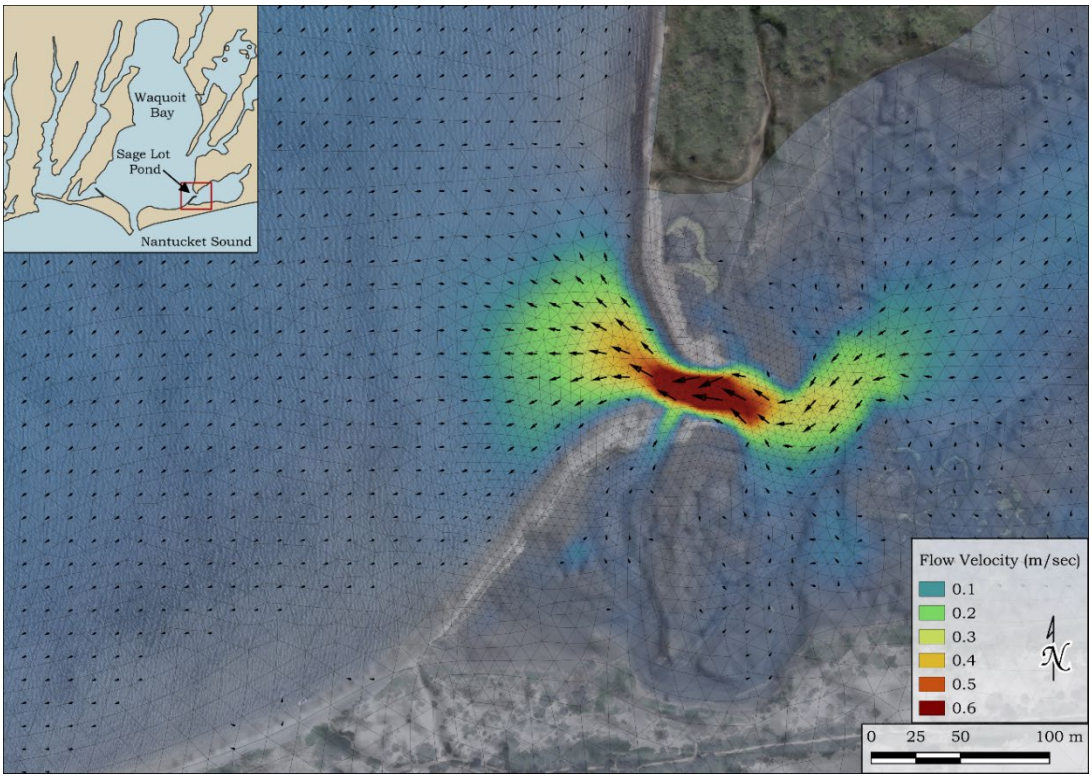

Figure 6.14 Example of model output at a time of maximum ebb currents at Sage Lot Pond.

7.0 Delft3D Integrated Flow and Wave Modeling (*Integrated Model*)

An integrated flow and wave model was developed for the Waquoit Bay system to capture the physical interaction processes between waves and hydrodynamics that are essential to computing sediment transport where waves contribute to the mobilization of sediment. The integrated model was developed using the calibrated Delft3D hydrodynamic model (D-Flow FM) coupled with the Delft3D Wave model (D-Wave) as part of the Delft3D D-Hydro Suite. The coupled Flow and Wave models operate independently, and transfer information via a communication file. The communication file translates velocity, bed level, and water level changes between the two model grids, throughout the duration of the simulation.

7.1. Wave Model Development

The wave component of the Delft3D integrated model utilized the SWAN (an acronym for Simulating WAves Nearshore) model to simulate refraction and shoaling induced by changes in bathymetry and by wave interactions with currents. The model includes a wave breaking model based on water depth and wave steepness. Model output includes significant wave height H_s, peak period Tp, and wave direction θ. SWAN is a flexible and efficient program based on the wave action balance equation that can quickly solve wave conditions in a two-dimensional domain using the iterative Gauss-Seidel technique (Booij et al., 1999). For this study, the model was implemented using a quasi-steady state finite-difference scheme, consisting on a locally refined irregular cartesian grid. The irregular cartesian grid allows for grid resolution refinement in shallow waters and areas of particular interest where accurate representation of bathymetric changes, depth influenced wave characteristics, and higher spatial variability in water surface elevation are important. An advantage of the iterative technique employed in SWAN is that it can compute spectral wave components for the full 360-degree compass circle.

The wave model grid requires a regular or curvilinear grid, consisting of an interpolated mesh of bathymetry. Geographical limits for the grid were chosen based on wave conditions selected for model simulations in order to ensure that larger waves were seaward of the depth of closure. The extent of the 161,920 wave grid nodes is shown in Figure 7.1. Each node represents a position where wave transformation calculations were computed by the Delft3D model. Special attention, in the form of grid resolution, was designated to the nearshore areas of Tim's Pond and Sage Lot Pond as well as the inlet to Waquoit Bay. Each model (hydrodynamics and waves) was developed independently; however, careful attention was made ensuring grid resolution was compatible in overlapping modeling regions.

A depth value was interpolated to each grid node from a combined topobathy dataset that included all sources from the hydrodynamic topobathy dataset. This dataset was interpolated to the grid using the Delft Quickin grid managing software to ensure appropriate depths for each grid node in the domain (Figure 7.2).

The model was run using a variable time step that was determined based on metrics of model stability (Courant number dependent on velocity, water depth, and grid cell size). The maximum model time step was set at 30 seconds, but that was reduced at times when the Courant number calculated for grid cells exceeded the threshold value of 1.

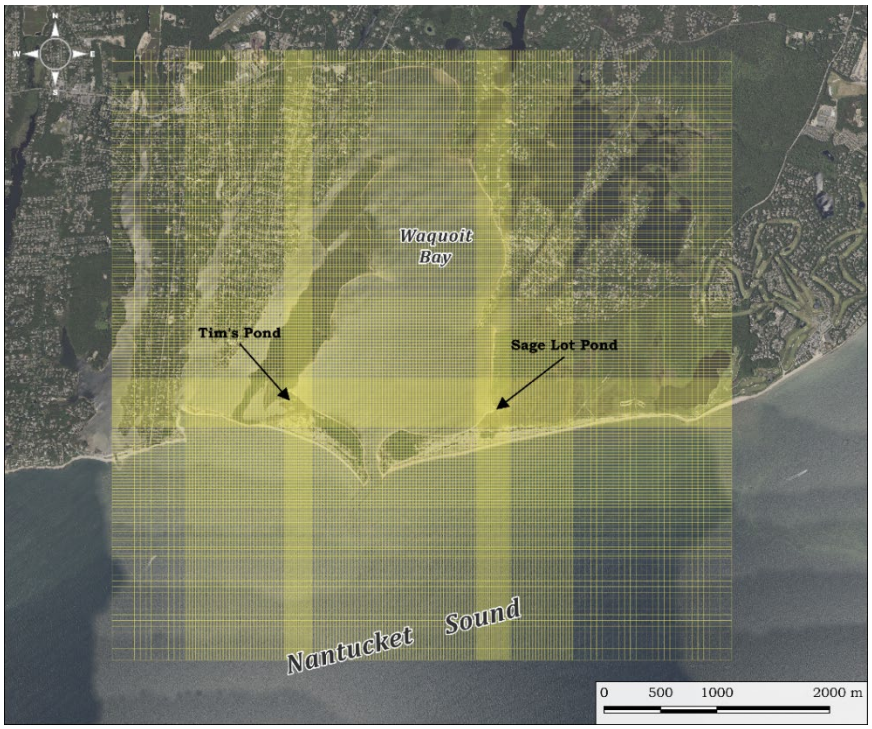

Figure 7.1 Map of Waquoit Bay with integrated wave model grid overlay. Grid resolutions increases incrementally from 100-, to 50-, to 20-, to 10-, to 5-meter grid spacing. The largest spacing occurs at the corners of the grid extent and the highest resolution is at the entrances of Tim's Pond and Sage Lot Pond.

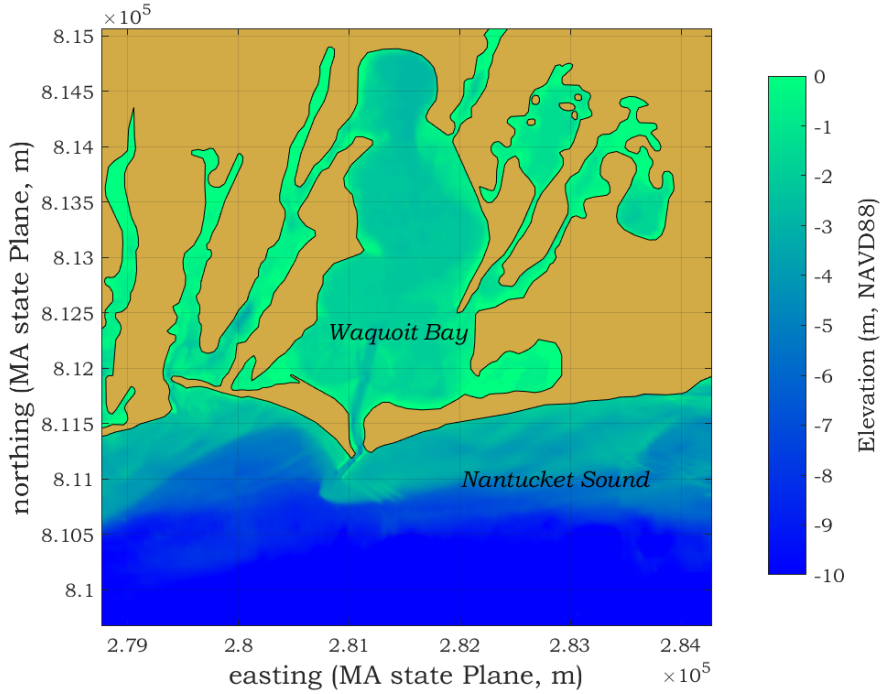

Figure 7.2 Color shaded plot showing the coverage of the Waquoit Bay wave model grid domain and bathymetry used in the model. The color shading represents the depth (in meters below zero NAVD88), transitioning from green to dark blue with increasing depth.

7.2. Wave Boundary Condition Development

Water waves are generated by gusts of wind that induce a drag across the ocean surface. Over time, persistent strong winds can generate relatively long wave lengths with large heights, replacing the less energetic waves initially created. Because wind patterns are complex, blowing in various directions with different speeds for varying amounts of time, the resulting sea typically is complicated as well. A useful simplification for studying ocean waves is to view the sea as a collection of single waves, each traveling in a different direction with a characteristic wavelength, height, and period. This concept of a wave spectrum makes the analysis of complicated seas possible, since the large numbers of individual waves may be viewed as groups of waves, each with similar height, period, and direction.

Due to the restoring force provided by gravity, ocean waves travel long distances across the surface of the ocean with relatively little change in shape. As waves travel, energy is exchanged between the different component waves of the spectrum, and a small amount of wave energy is dissipated through surface tension and white capping. However, the waves in the open ocean remain fairly uniform as they travel through deep water. As the waves propagate into intermediate and shallow water depths, the presence of the bottom begins to alter the wave's speed, height, and direction.

As a wave propagates into water of decreasing depth, the wave length decreases while the wave period remains constant. Wave period is defined as the time required for successive wave crests to pass a particular location. Consequently, waves travel at slower speeds in shallow water. This process causes wave crests to bend, or refract, toward regions of shallow water and away from regions of deep water. The crests of waves approaching the shoreline at an angle become more parallel to the shoreline as the water depth decreases. Refraction also serves to focus wave energy on headlands, reefs, and shoals, while diverting energy from deep holes and channels. This, in turn, impacts the shape and size of fully developed waves propagating across Nantucket Sound. In addition, the geography of Nantucket Sound tends to directly block a much of the wave energy propagating from the south due to Marthas Vineyard and Nantucket, which increases the complexity of identifying the specific combination of conditions that influence different regions of the South Cape shoreline.

7.2.1. Wave Generation

To accurately introduce the wave forcing conditions along the open boundary of the integrated model, a separate, larger scale (regional), standalone SWAN model was developed to encompass Nantucket Sound. The regional scale model allows for waves measured offshore to propagate across Nantucket Sound as well as generation of wind-waves within the sound and apply the appropriate wave transformation along the boundary of the integrated model. The integrated model utilizes the wave output from the regional grid for the boundary conditions.

The regional SWAN model developed for Nantucket Sound used a coarse grid resolution with 100-meter spacing extending to the south of Marthas Vineyard and Nantucket, east of Monomoy, and west of the Elizabeth Islands (Figure 7.3). Wind data from the NOAA NDBC Nantucket Sound buoy (Station 04420) and wave data from WIS hindcast stations along the eastern, southern, and western extents of the model (Stations 63071, 63082, and 63074) were used as the input forcing conditions for the regional model. The x- and y- axis of the regional grid are approximately 53 and 88 kilometers (or 531 and 881 cells) long, respectively. The x-axis is oriented to the east. The greatest depth in the domain is

approximately -42 meters NAVD88, which occurs near the open boundary southwest of Marthas Vineyard. The ninth arc-second resolution Continuously Updated Digital Elevation Model (CUDEM) produced by NOAA National Centers for Environmental Information (NCEI) was the main source of bathymetric information interpolated to the grid (Figure 7.4).

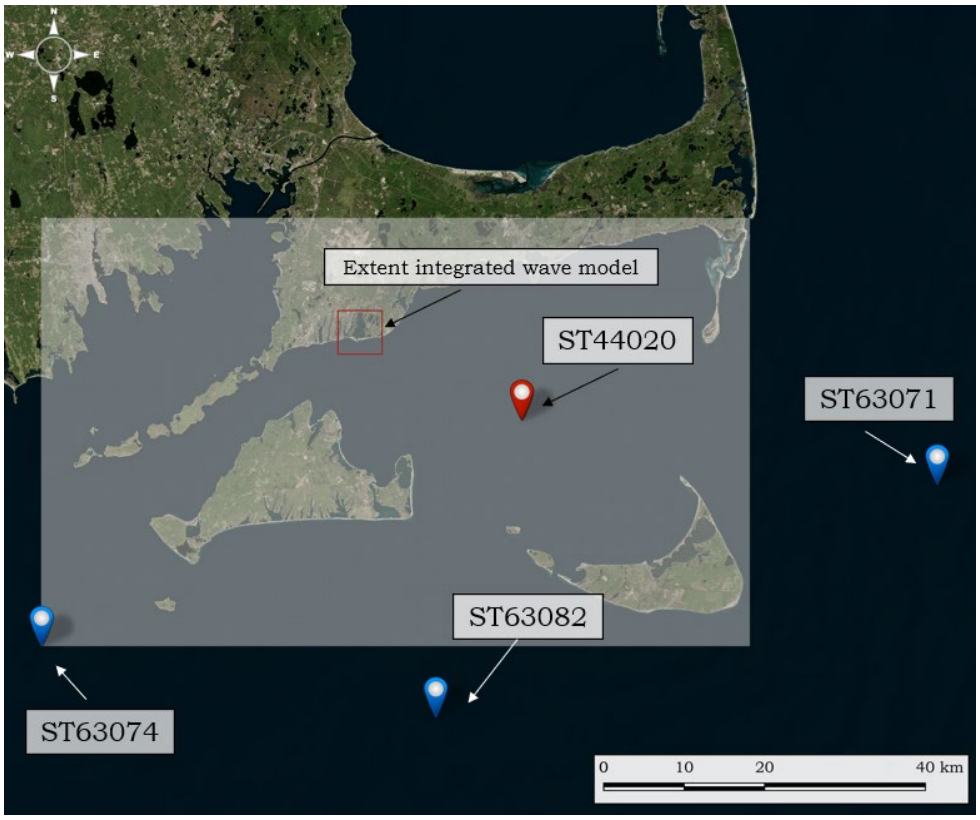

Figure 7.3 Map showing the standalone wave model domain as well as the location of NDBC Nantucket Sound Buoy (44020); WIS hindcast stations 63074, 63082, and 63071; and the extent of the integrated wave and hydrodynamic model grid for Waquoit Bay.

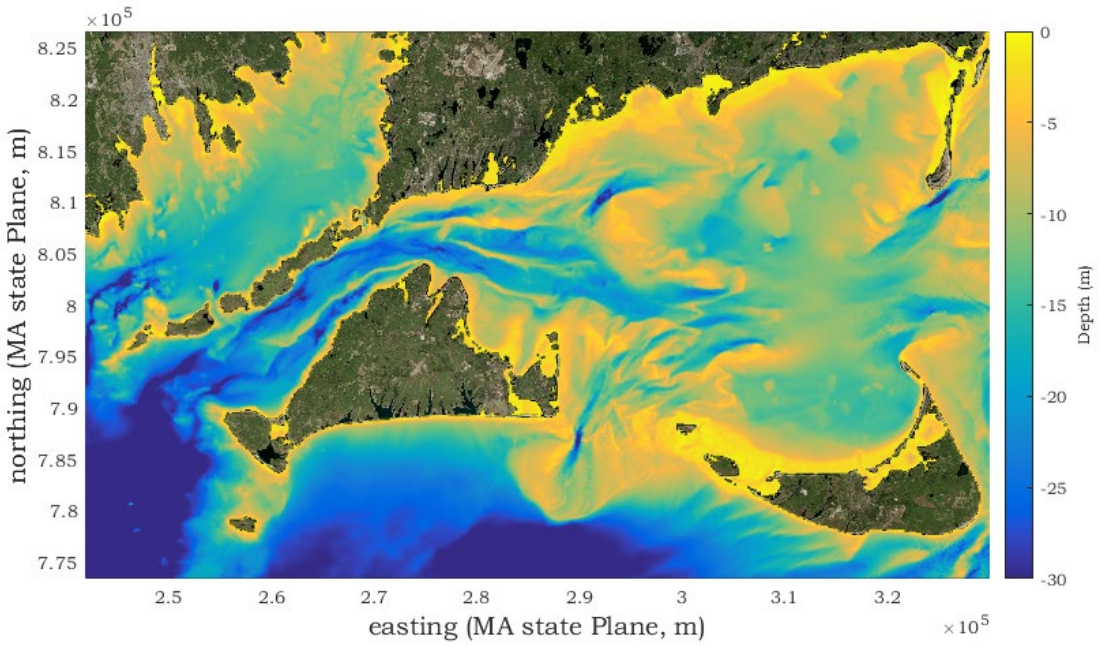

Figure 7.4 Extent of the standalone SWAN wave model grid, with interpolated bathymetry.

7.3. Model Run Case Development

Long-term modeling of the annual conditions experienced by the Waquoit Bay system was unfeasible with the size of the grid, and the timescales of the temporal variability influencing sediment transport in the areas of Tim's Pond and Sage Lot Pond. Therefore, short (on the order of a few days) episodic events, generating the greatest opportunity for sediment transport into the ponds, were determined to be sufficient to evaluate the conditions governing sediment mobilization and transport patterns. For the purpose of this work, energetic wave conditions and high water levels consistent with winter storms were determined to provide the best opportunity for short term transport into the ponds.

Due to the orientation of the inlets between Waquoit Bay and both Tim's Pond and Sage Lot Pond, two differently directed historical winter storms were modeled to evaluate the relationship between storm surge inundation and the influence of locally developed wind-driven waves on sediment mobility and deposition within the marsh for each of the ponds. Winter Storm Grayson (January 4-7, 2018) consisted of primarily northerly winds which results in larger nearshore wave heights in the southern end of Waquoit Bay (Figure 7.5). However, the storm presented a short duration storm-surge that only lasted approximately one tide cycle. Winter Storm Elliott (December 22-25, 2022) was a southerly winter storm that consisted of high winds coming from the southeast and southwest directions (Figure 7.6). Unlike with Winter Storm Grayson, the storm surge generated by Winter Storm Elliot lasted much longer (approximately two tide cycles) and coincided with astronomically higher tides before and after the storm.

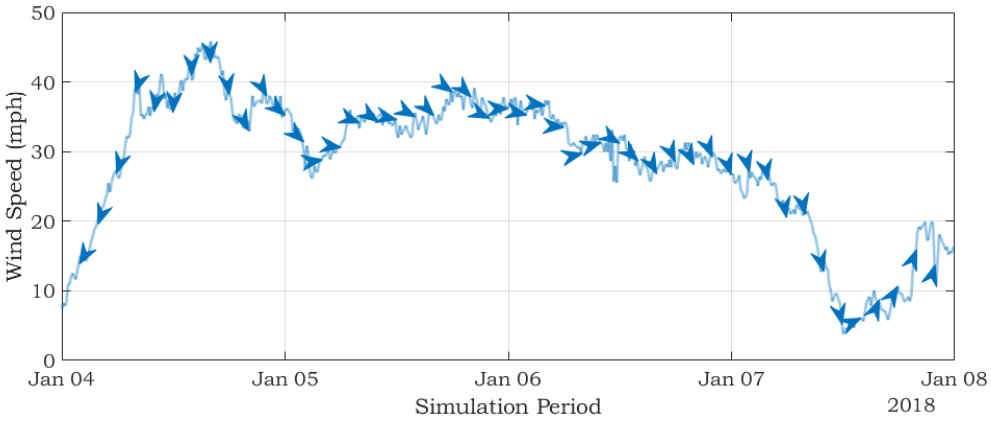

Figure 7.5 Wind data from Winter Storm Grayson (2018), obtained from NDBC Nantucket Sound Buoy (Station 44020), used to simulate northerly storm conditions experienced in Waquoit Bay.

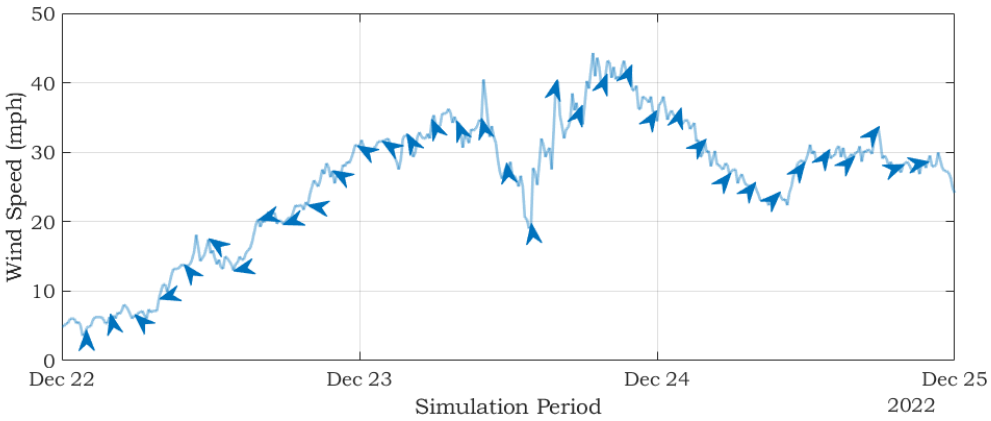

Figure 7.6 Wind data from Winter Storm Elliott (2022), obtained from NDBC Nantucket Sound Buoy (Station 44020), used to simulate northerly storm conditions experienced in Waquoit Bay.

7.3.1. Tides and Water Levels

To construct accurate water levels as the boundary condition for the hydrodynamic model during these simulations, synthetic tidal forcing was developed using tidal data from the NOAA tide gauge at Woods Hole and the tide data used in the calibration of the hydrodynamic model. The water level measurements from Woods Hole were deconstructed to extract the meteorological and astronomical components of the tide signal. The specific phase and periodic cycle of the astronomical tide during the simulation period was aligned to the tides during the calibration period using a cross-correlation process. A time lag in tide phase between Woods Hole and Waquoit Bay during the calibration period was determined and applied to the storm surge levels for the simulation period extracted from Woods Hole. The constructed tide signals applied to the offshore boundary of the model for Winter Storm Grayson and Winter Storm Elliott are shown in Figure 7.7 and Figure 7.8, respectively.

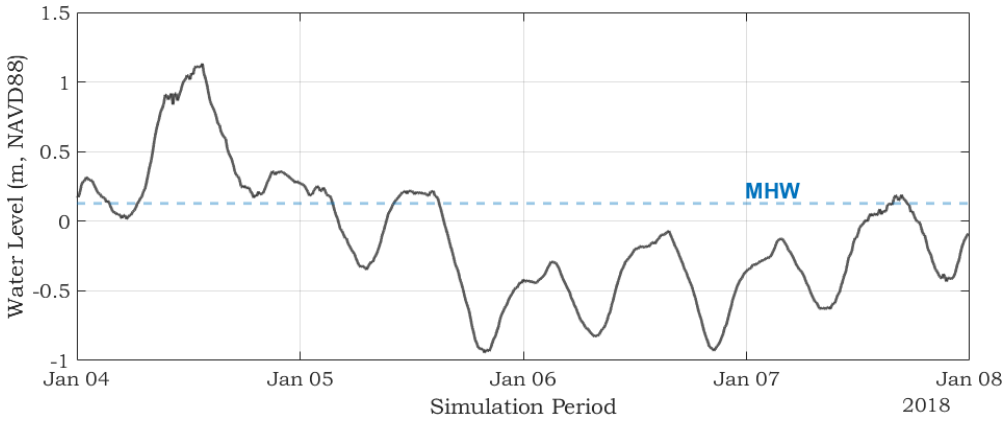

Figure 7.7 Water levels used as the offshore hydrodynamic forcing conditions for the simulation of Winter Storm Grayson (2018).

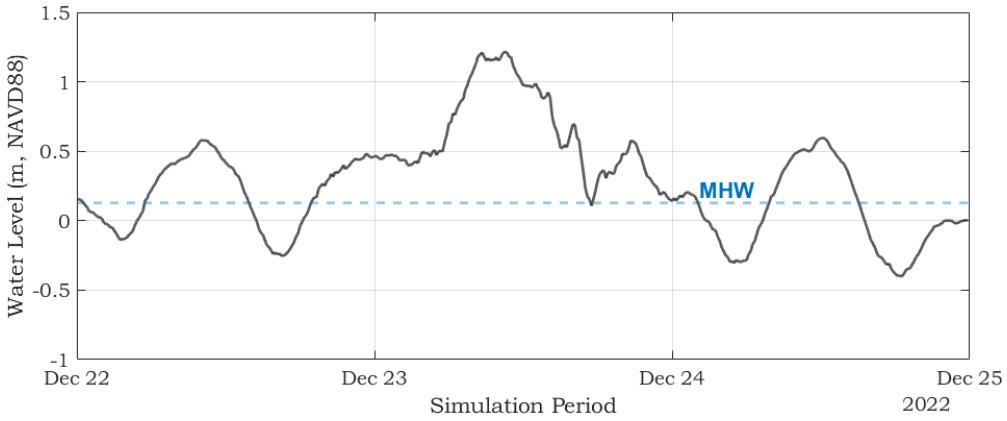

Figure 7.8 Water levels used as the offshore hydrodynamic forcing conditions for the simulation of Winter Storm Grayson (2018).

7.4. Model Validation and Results

The model output from the regional wave model was validated using wave heights measured by the NOAA Nantucket Sound buoy (Station 44020) for each of the simulation periods to ensure wave propagation and generation in Nantucket Sound was being accurately represented in the model (Figure 7.9 and Figure 7.10). The modeled waves in the regional grid generally show a good correlation to the measured wave data. However, the largest waves measured during the simulation periods were not well resolved by the model, likely due to depth limited wave heights influenced by the shallow waters on the shoals in Nantucket Sound. Peak significant wave heights recorded by the NOAA buoy during Winter Storm Grayson and Winter Storm Elliott coincide with water levels above MHW; however, comprehensive tide data for the area encompassed by the regional wave grid was not available for the simulation periods, therefore water levels used in the standalone wave model were set to zero feet (NAVD88). The effects of these shoals can be observed in Figure 7.11 and Figure 7.12, where wave heights are reduced in the shallow water areas of Muskeget Channel to the south, between Monomoy and Nantucket to the east, and on Horseshoe Shoal in the vicinity of the NOAA Buoy. Due to the absence of shallow water shoals in the vicinity of the offshore

boundary of the integrated Waquoit Bay model, the influence of water levels for wave generation as a boundary condition was considered negligible as the wave heights used to force the integrated hydrodynamic and wave model were combined with local tides and storm setup.

Although waves within Waquoit Bay were shown to reach a maximum height of almost 0.8 meters, results of the integrated hydrodynamic and wave model for Waquoit Bay show that waves in Nantucket Sound and Vineyard Sound have relatively negligible influence on the wave conditions within the embayment system. Due to the curving geometry and constriction of the Waquoit Bay and Eel River inlets, waves entering the embayment are attenuated substantially through the length of the inlet (Figure 7.13). Waves propagating through the Waquoit Bay inlet generally experienced a reduction in height by a factor of 5. Specifically, for the 2018 and 2022 storm scenario simulations, the average wave energy dissipation through the Waquoit Bay inlet was 96% and 97%, respectively. Thus, indicating that the waves within the system are generated locally, and limited by the depth or fetch of Waquoit Bay.

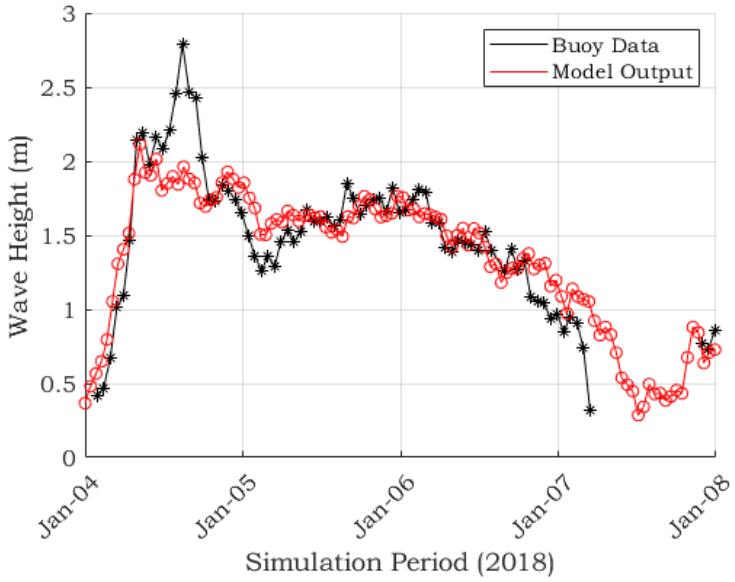

Figure 7.9 Comparison of wave heights measured at the NDBC Nantucket Sound buoy (Station 44020) and output wave heights from the standalone Nantucket Sound SWAN model during Winter Storm Grayson (2018).

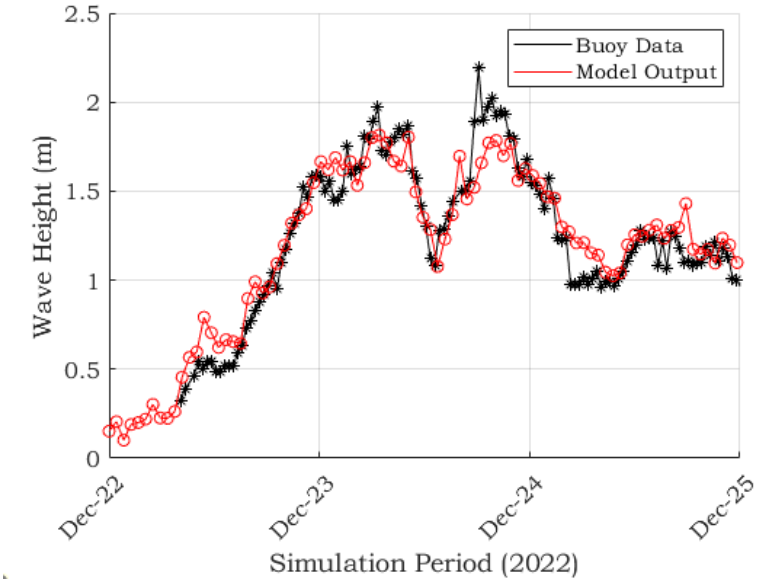

Figure 7.10 Comparison of wave heights measured at the NDBC Nantucket Sound buoy (Station 44020) and output wave heights from the standalone Nantucket Sound SWAN model during Winter Storm Elliot (2022).

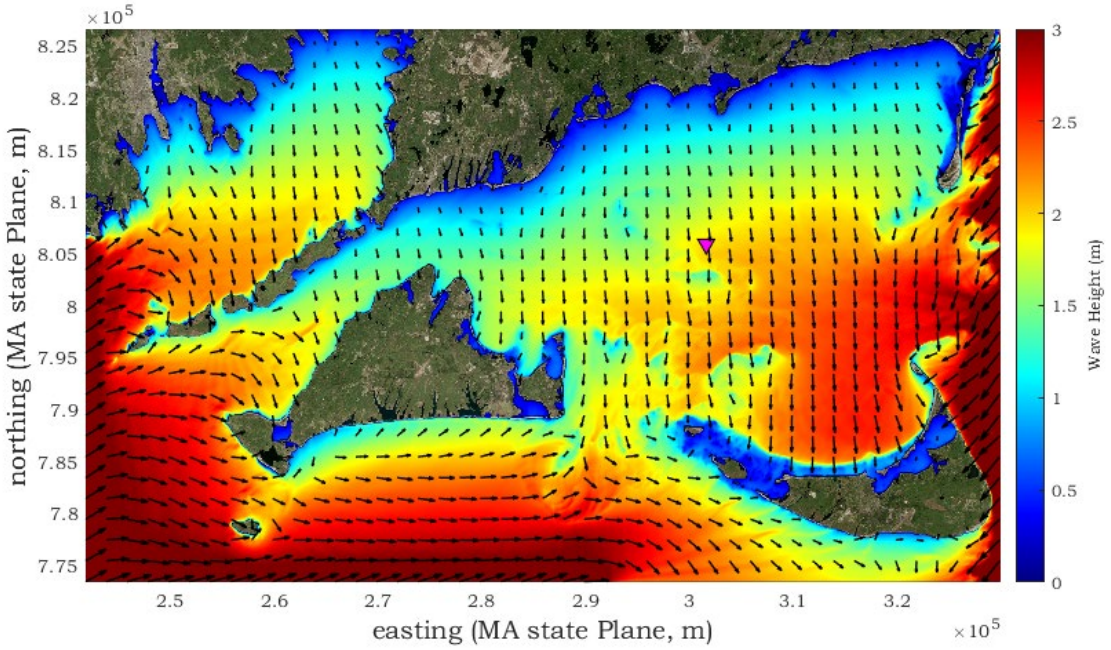

Figure 7.11 Model output of significant wave height in meters within the domain of the regional standalone wave model corresponding to when largest waves were measured during Winter Storm Grayson (approximate time step: January 4, 2018 15:40 EST). NOAA Buoy (Station 44020) location is represented by magenta triangle.

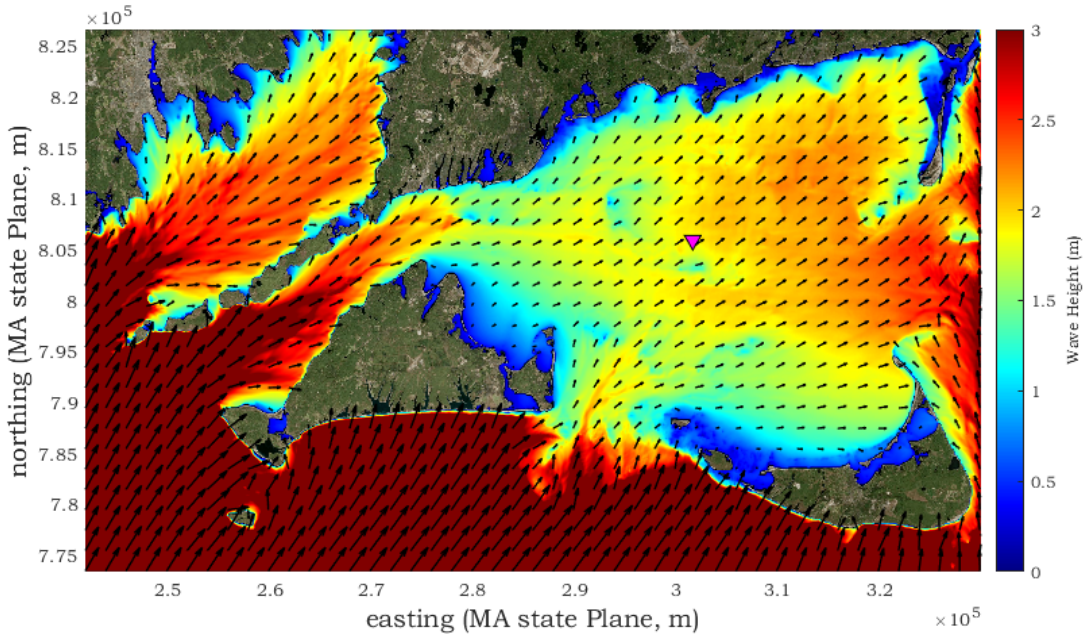

Figure 7.12 Model output of significant wave height in meters within the domain of the regional standalone wave model corresponding to when largest waves were measured during Winter Storm Elliott (approximate time step: December 23, 2022 17:50 EST). NOAA Buoy (Station 44020) location is represented by magenta triangle.

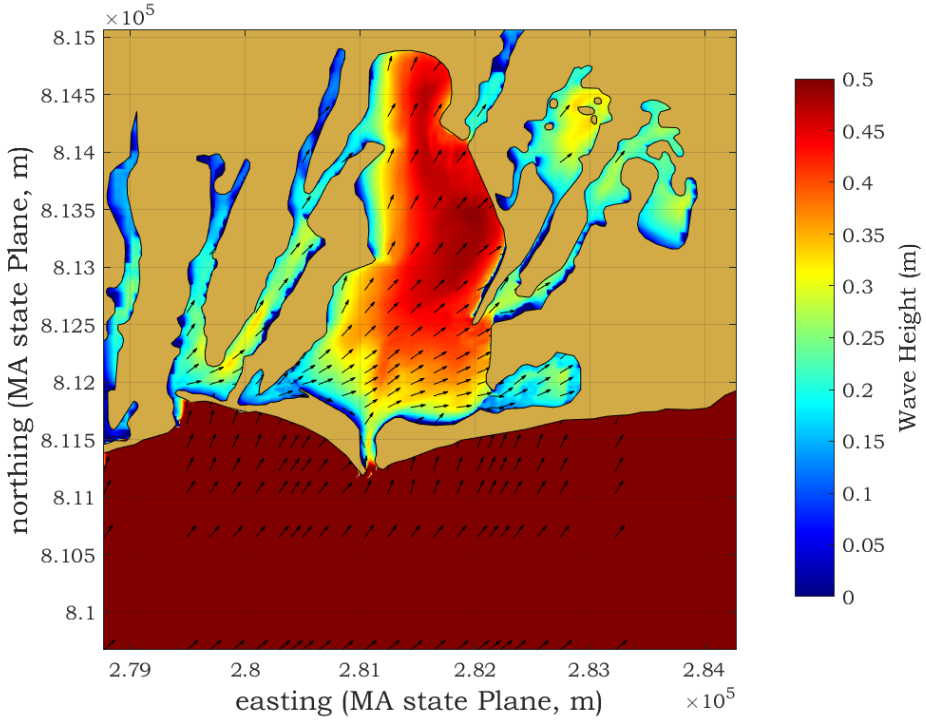

Figure 7.13 Model output of significant wave height in meters within the domain of the integrated hydrodynamic/wave model corresponding to when largest waves were measured during Winter Storm Elliott (approximate time step: December 23, 2022 17:50 EST).

8.0 Sediment Transport Modeling

Sediment transport in Waquoit Bay was simulated using a coupled wave-current-sediment transport modeling framework. The Coupled-Ocean-Atmosphere-Wave-Sediment Transport (COAWST) modeling system brings together existing open-source models to allow for interaction between processes in the constituent models (Warner et al., 2010). The circulation model is the Regional Ocean Modeling System (ROMS), which solves the 3-d Reynolds-averaged Navier-Stokes equations on a curvilinear finite difference grid with stretched terrain-following vertical coordinates (Shchepetkin and McWilliams, 2005; Haidvogel et al., 2008). Surface gravity waves are modeled with Simulating Waves Nearshore (SWAN), a spectral model of wave action density that accounts for refractive propagation and energy dissipation over bathymetry (Booij et al., 1999). The Community Sediment Transport Modeling System (CSTMS) simulates multiple sediment size classes, accounting for sediment settling in the water column and vertical exchange with the bed through erosion and deposition (Warner et al., 2008). The models are coupled through the Model Coupling Toolkit (Larson et al., 2005). Mean water levels and currents influence the wave propagation, and waves orbital velocities influence the total bottom stress and sediment resuspension. All the models use the same horizontal grid.

The model grid for Waquoit Bay was designed to focus grid resolution in the lower parts of the bay to better represent the bathymetry and currents near Sage Lot and Tim's Ponds (Figure 8.1). In this lower part of the bay, the horizontal grid resolution is about 5-6 m. The vertical dimension has sigma-coordinates with 10 evenly spaced levels. Model bathymetry was interpolated from USACE lidar surveys (2018), and where that was not available, from the NOAA Continuously Updated Digital Elevation Model. Shipboard bathymetric surveys during this study found satisfactory agreement with the lidar data in the ponds and the shallow regions just outside of the ponds, with differences that were typically around 10 cm and no clear biases. The lidar data cuts out at depths greater than about 1.1 m, leaving just a few small gaps in coverage in the ponds that were filled with the other sources. Boundary conditions for the circulation model are based on harmonic predictions of tidal water level for Vineyard Sound plus the low-frequency (non-tidal) component of observed water level at the NOAA gauge at Woods Hole (Station 8447930). Wind forcing for the circulation and wave models is taken from observations at the NDBC buoy in Nantucket Sound (Station 44020). For the wave model, no waves are imposed at the open boundaries in Vineyard Sound because the regional-scale wave modeling (see Section 7.4) found that offshore waves don't substantially affect conditions in Waquoit Bay, and instead the wave field inside the bay is locally generated.

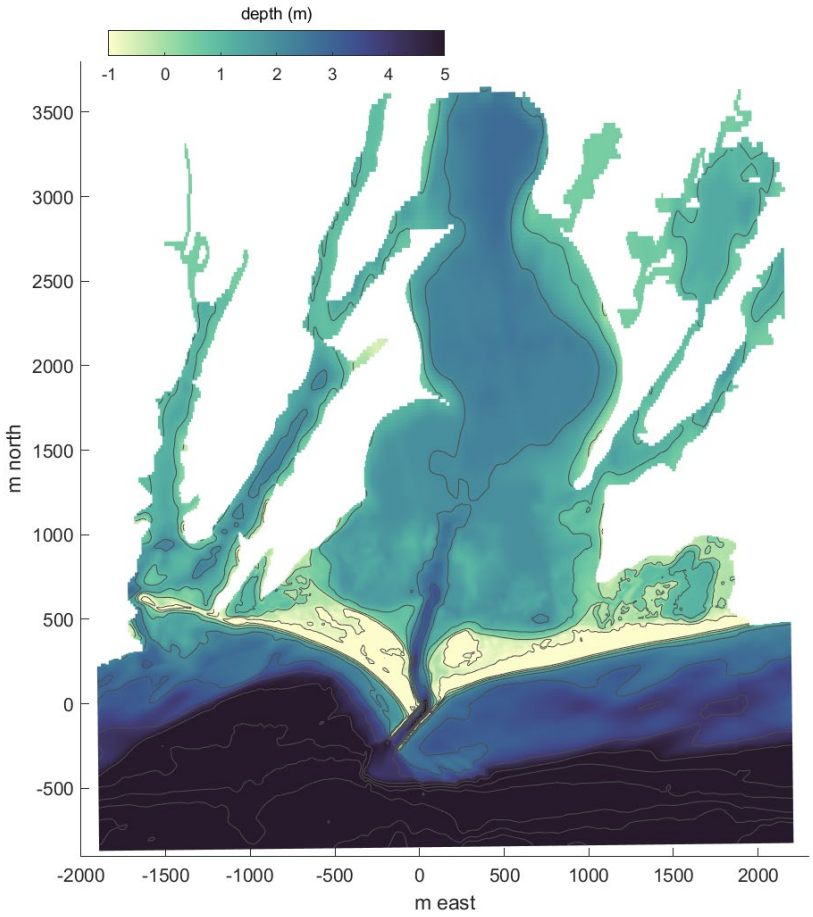

Figure 8.1. Sediment model grid extent and bathymetry.

Table 8.1 Sediment classes in model

Sediment class	Diameter (μm)	Settling velocity (mm/s)	Critical stress (Pa)	PSA fraction (%)
Medium sand	500	60	0.25	0
Very fine sand	100	5.0	0.20	40
Coarse silt	40	1.0	0.16	30
Medium silt	20	0.3	0.16	30

Sediment in the baseline model cases is represented in four discrete size classes (Table 8.1). The sediment size classes are chosen to represent the range of sediment types observed from the particle size distributions of the grab samples (Fig. 5.8). Nominally, the size classes are medium sand (500 μm diameter), very fine sand (100 μm), coarse silt (40 μm), and medium silt (20 μm). The observed particle size distributions include bed sediment both finer and coarser than these classes, but these sizes represent much of the range. In the grab samples, an inverse relationship between the water depth and fine faction (diameter < 63 μm) was observed – i.e., the shallower regions at the edges of the bay were sandier than the deeper central basin (Figure 8.2). Based on these observations, water depth in the model was used to

initialize the bed sediment composition. The model was then run for a spin-up period of about 10 days with storm forcing conditions, and the bed was allowed to evolve. The bed sediment distribution at the end of the spin-up period was then used to initialize subsequent model simulations (Figure 8.2).

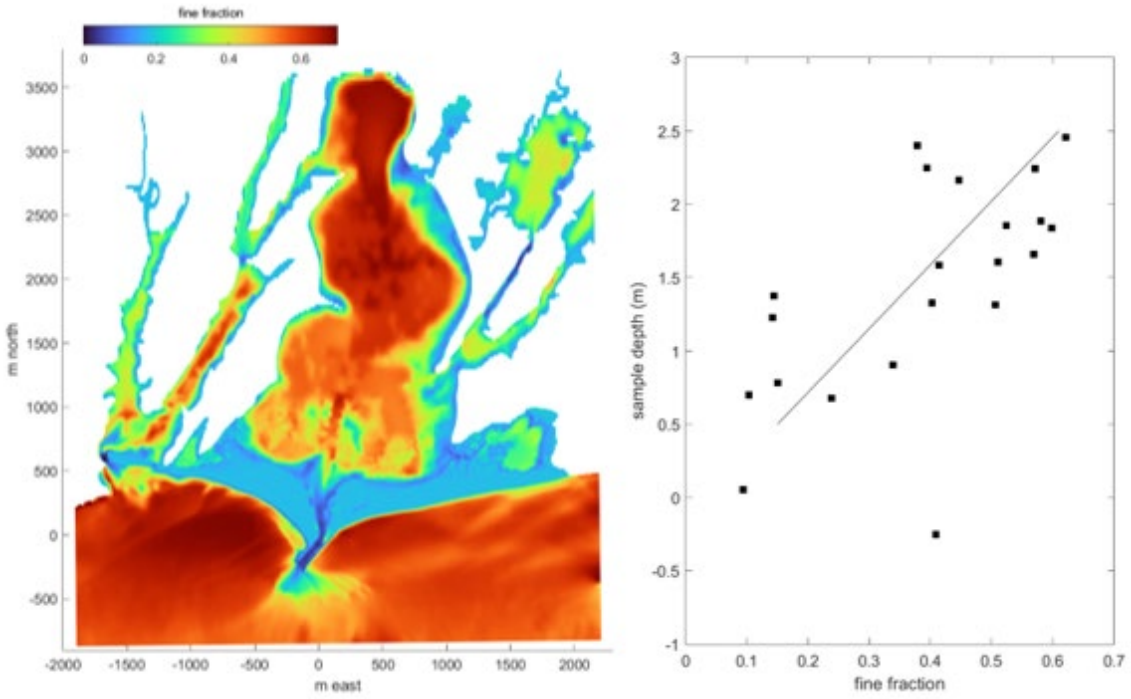

Figure 8.2 (left) Bed sediment for the baseline cases. Bed composition is initially prescribed based on water depth and a linear fit of the grab samples (right panel). The bed evolves over a spin-up period of about 10 days, and the bed at the end of the spin-up (shown here) is used to initiate the model runs.

Sediment transport simulations were run for several sets of forcing conditions. As described above (Section 7.3), two winter storm periods with different characteristic wind conditions were simulated. During the January 4-8, 2018 event, winds were 15-20 m/s and predominantly from the north, starting from the northeast and then switching to from the northwest. For the December 22-25, 2022 event, winds were 12-18 m/s and from the south, initially from the southeast and then from the southwest. Model simulations were also run for the period of field observations in 2023. A two-week period in March 2023 that had several moderate wind events was simulated, along with a shorter period in May with weaker wind forcing. Model results were compared with observations for water levels, wave height, currents, and suspended sediment concentrations.

Results from sediment transport model cases are shown to illustrate the conditions in and near the ponds during different forcing conditions. For example, the May 3-7, 2023 period had moderate wind conditions that were initially from the south and then turned to being from the north. Time series are shown from the model at locations corresponding with the instruments during the observations: outside Tim's Pond and Sage Lot Pond and in the entrance channel to each pond (Figure 8.3). The tidal range during this period was about 0.4 m. Early in the period, a mean water level setup increased water levels by about 0.2 m, and the

water levels fluctuated together at all the sites with the tides. After the wind switched around, mean water levels decreased to around MSL. With less surge, water levels around low tides were higher in the pond channels than at the locations just offshore due to the friction of the shallow flows draining the ponds.

On May 3rd when the wind was from the south the wave heights were small due to the limited fetch at the ponds and the modest wind speeds (Figure 8.3). On May 4th when the winds started coming from the north, wave heights increased to about 20 cm outside the ponds but were less than half that in the entrance channels. The increase in waves corresponded to increased suspended sediment concentrations. Outside the ponds, SSC was 20-30 mg/L, and in the entrance channels concentrations were lower. This is in sharp contrast to the start and end of this period when suspended sediment concentrations outside the ponds were near zero. Although the wind forcing was modest compared to typical storm events, these results illustrate that waves rather than tides are the dominant means for sediment resuspension in the system.

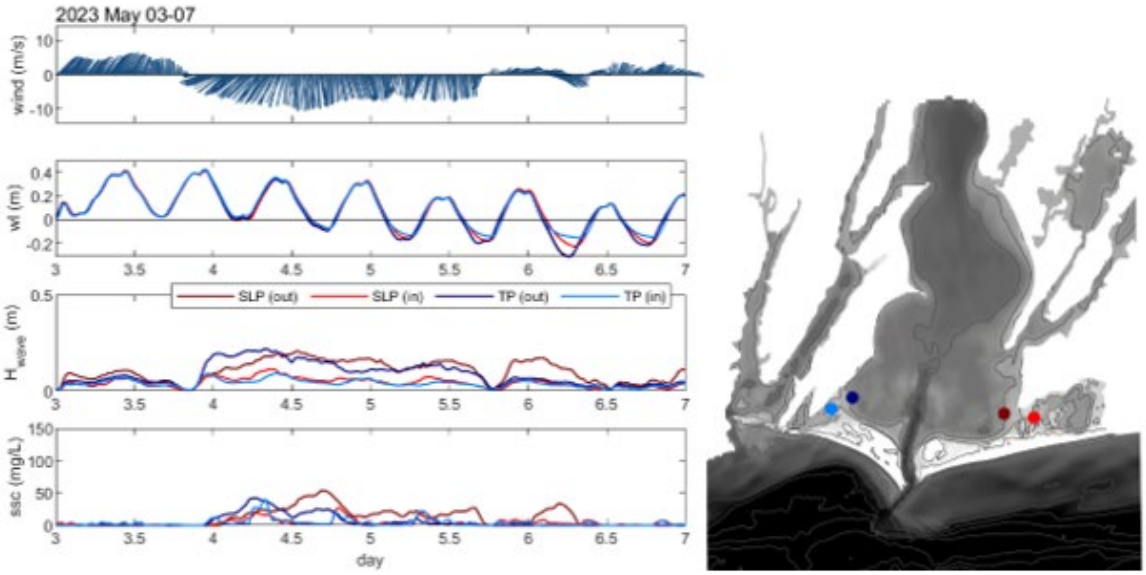

Figure 8.3 (left) Time series from the sediment transport model for May 03-07, 2023. (top panel) Wind vectors, showing direction wind is toward. (lower panels) Water level, wave height, and SSC at locations just outside Sage Lot Pond (SLP) and Tim's Pond (TP) and in the entrance channels to each pond. (right) Map showing locations of time series (colors of dots correspond to lines in plots).

An example of model results from a larger wind event is shown for December 22-25, 2022 (Figure 8.4). During the storm, winds were initially from the southeast before switching to southwesterly. The storm resulted in a substantial mean water level setup in the bay, with a total water elevation of over 1 m around its peak. Spatial variability in the wave heights responded to the shift in the wind direction. Early in the event, wave heights were over 30 cm outside Tim's Pond, and waves on the west side of the bay were more than twice as big as waves on the east side due to the greater fetch with the wind from the southeast. Wave heights were also modulated by water depth, increasing when water levels increased due to the mean set-up and the tide. Around mid-day on the 23rd, the wind shifted and waves became larger outside Sage Lot Pond on the east (downwind) side of the bay. For the rest of the period

shown, the wind from the southwest resulted in a greater fetch for Sage Lot than Tim's, and waves were 20-30 cm, with the wave height modulated by the tidal water level.

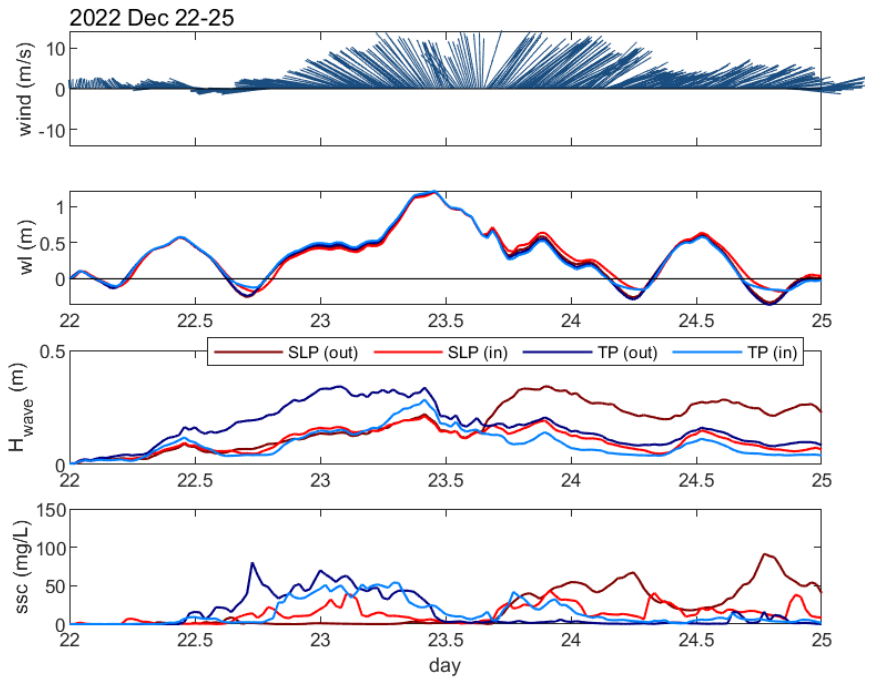

Figure 8.4 Time series from the model for December 22-25, 2022. (top) Wind vectors, showing direction toward. (lower panels) Water level, wave height, and SSC at locations outside and in the channels to Sage Lot Pond (SLP) and Tim's Pond (TP). See Figure 8.3 for map of station locations.

Suspended sediment concentrations closely correspond to the wind and wave conditions at the two ponds (Figure 8.4). Early in the December 2022 event, SSC increased to about 50 mg/L outside Tim's Pond when wind was from the southeast. SSC in the entrance channel to Tim's Pond was similar to that outside, indicating that sediment resuspended by waves in the shallow region offshore was being carried into the pond by the rising water levels due to the mean set-up and flood tide. Note that during this early period, SSC outside Sage Lot Pond was nearly zero due to the limited fetch and small waves. SSC was about 20 mg/L in the entrance channel to Sage Lot, likely due to resuspension with increased velocities in the channel with the flooding storm surge. After the wind switched to southwesterly, SSC outside Sage Lot Pond increased to about 50 mg/L along with the increase in wave height. Sediment concentrations in the channel to Sage Lot also increased, but were generally less than half the SSC outside the pond. Modest increases in the SSC going in the channel to Sage Lot corresponded with the start of flood tide (e.g., day 23.4 and 23.9), but the lower surge levels during the later parts of the storm limited the transport of sediment resuspended offshore of Sage Lot into the pond.

Model results from January 4-8, 2018, illustrate the response of the system to a strong wind event from the north (Figure 8.5). Winds were initially from the northeast, and after about a day became northwesterly. Storm surge peaked at about 1 m above MSL around the time of the wind shift. Mean water levels subsequently decreased to below MSL (i.e., set-down), and the tidal water levels outside the ponds were below the water levels in the ponds.

As with the December 2022 storm, the changes in wind direction affected the spatial patterns of waves and SSC. When wind initially from the northeast, wave heights were 40 cm outside Tim's Pond and SSC was about 100 mg/L. When the wind shifted to being from the northwest, wave heights and SSC decreased outside Tim's and increased outside Sage Lot Pond. Wave heights were modulated by the changes in mean and tidal water level, increasing when water levels were higher and larger waves could propagate closer to the shoreline. SSC outside Sage Lot remained elevated for several days with the persistent westerly wind. However, sediment concentrations in the channel to Sage Lot were much lower than in the bay outside. During this period, water levels outside the pond were lower than inside due to the large-scale set-down, so consequently, little of the sediment suspended offshore was transported into the pond.

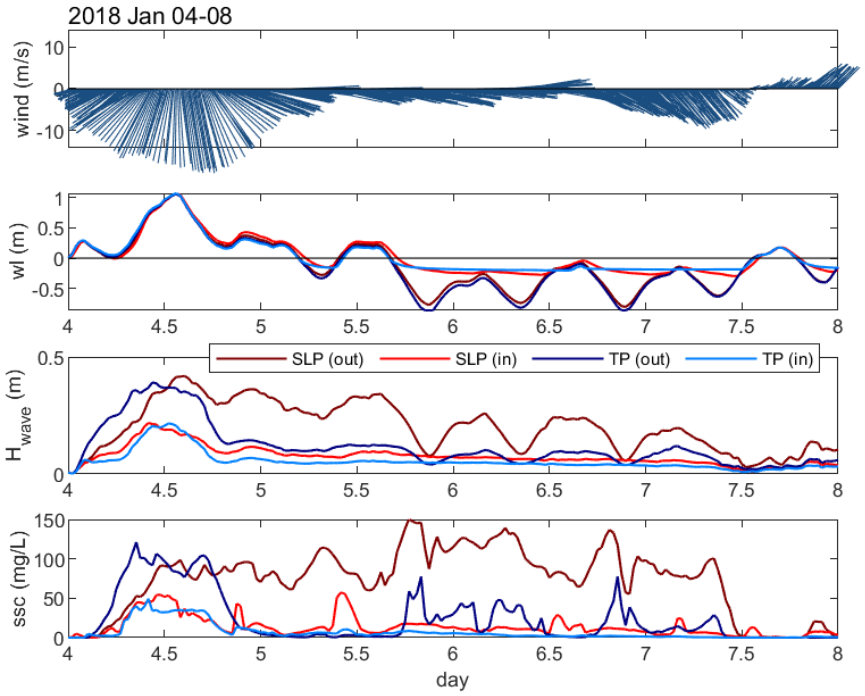

Figure 8.5 Time series from the model for January 4-8, 2018. (top) Wind vectors, showing direction toward. (lower panels) Water level, wave height, and SSC at locations outside and in the channels to Sage Lot Pond (SLP) and Tim's Pond (TP). See Figure 8.3 for map.

The sediment transport modeling reinforced many of the findings from the observations. Wave heights during storm events are modest (20-40 cm), but the wave stresses are important for resuspending sediment. Tidal currents are weak near the ponds and don't generate large enough bed stresses to resuspend sediment except in the channels connecting the ponds to the bay. Waves are locally generated rather than propagating in from outside Waquoit Bay, so the wind direction and corresponding fetch plays a primary role in determining the spatial distribution of waves and sediment resuspension. Events with strong winds also cause changes in mean water level that can be similar to or greater than the tidal range. Wind from the east typically corresponds with storm surge and increased water level, whereas wind from the west tends to have lower mean water levels. Due to the small tidal range, the correlation between wind direction and storm surge can play a significant role in

determining whether sediment resuspended in the shallow regions offshore of the ponds is transported into the ponds and onto the marsh. In the events examined here, Tim's Pond on the west side of the bay tends to have larger waves and higher SSC during the easterly winds with the greatest storm surge, whereas the westerly exposure of Sage Lot Pond results in less correspondence between the periods of large waves and high water level, and thus less sediment transport into the pond.

8.1. Passive Sediment Augmentation Model Results

Model simulations were run to evaluate how Passive Sediment Augmentation might influence sediment distributions in the estuary. The aim was to simulate placement of dredged material in shallow, subtidal regions offshore of Tim's and Sage Lot Ponds. The dredged material would be relatively fine-grained so that the sediment placement could be resuspended during storm events and transported to the ponds and surrounding marshes. The design of the sediment placement in these simulations is an initial scenario that could be refined and optimized with additional analysis.

Sediment placement areas for the PSA simulations were specified as rectangular areas outside the mouths of Tim's and Sage Lot Ponds (Figure 8.6). Initial water depths in the placement areas are 0.6-1.4 m, and the bottom sediment in these locations is sandy due to the influence of waves on sediment resuspension (Figure 8.2). The sediment placements are piles of sediment that are assumed to take up half the water depth, such that the modified water depths in the placement areas are 0.3-0.7 m. Sediment composition of the placement material is assumed to be predominantly fine-grained: 30% medium silt, 30% coarse silt, and 40% very fine sand. The placement sediment classes are tracked separately from the bed material but otherwise have the same properties as the three finest grained classes in the baseline cases (Table 8.1). The composition of the sediment placement is consistent with the bed sediment in the deeper parts of Waquoit Bay, e.g., in the channel between the northern and southern basins of the bay that has previously been dredged. The total volume of sediment in the placement areas with this configuration is about 28,000 cu-yd. For context, we estimate that the total volume of sediment accumulating annually in Waquoit Bay to keep up with sea level rise (about 3 mm/y) is similar, at about 27,000 cu-yd.

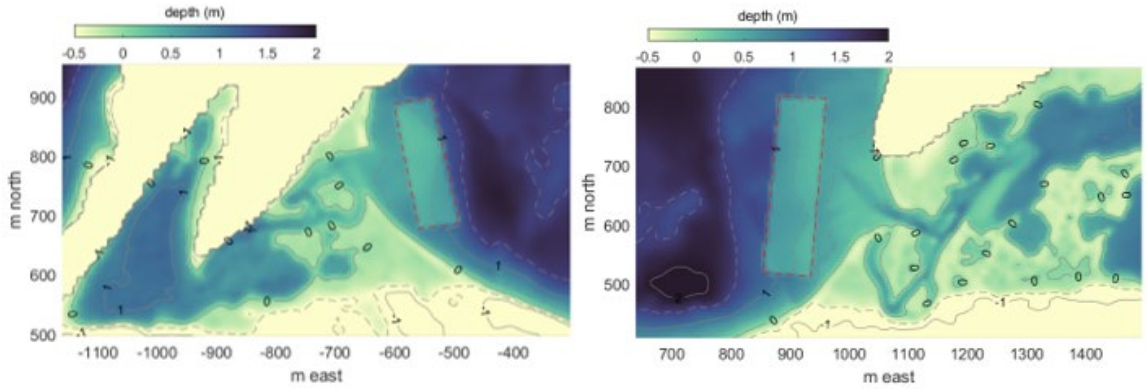

Figure 8.6 Model bathymetry with modifications for PSA placement outside (left) Tim's Pond and (right) Sage Lot Pond. Red dashed lines show PSA placement regions.

To examine the response of the PSA sediment placements to a range of forcing conditions, the modified bathymetry was run for the storm events of January 2018 (Figure 8.5)

and December 2022 (Figure 8.4), as well as for a two-week period during the observations in March 2023. The wind and water level conditions during the March 13-27, 2023 period were representative of typical winter and spring conditions, with a series of moderate storm events (Figure 8.7). As with the examples shown above, the wave heights and suspended sediment concentrations outside the ponds were strongly correlated. Storm events at the beginning and end of the simulation period show similar patterns, with initially easterly wind causing larger waves and greater SSC near Tim's Pond before switching to westerly winds with greater waves and SSC near Sage Lot Pond. As in the January 2018 and December 2022 events, storm surge caused variations in water level that were similar to the tidal range, and maximum storm surge corresponded with the easterly wind. The results shown for the PSA simulation have suspended sediment concentrations offshore of the ponds that are 200-400 mg/L, which is greater than the SSC in the baseline cases. The locations of the plotted time series are in the sediment placement regions, so the greater SSC reflects the increased availability of fine-grained sediment for resuspension during wave events. Sediment concentrations in the channels into the ponds are substantially lower than outside the ponds and are modulated by the tidal currents, reflecting transport of sediment resuspended from the PSA areas into the ponds that depends on the tidal currents and surge.

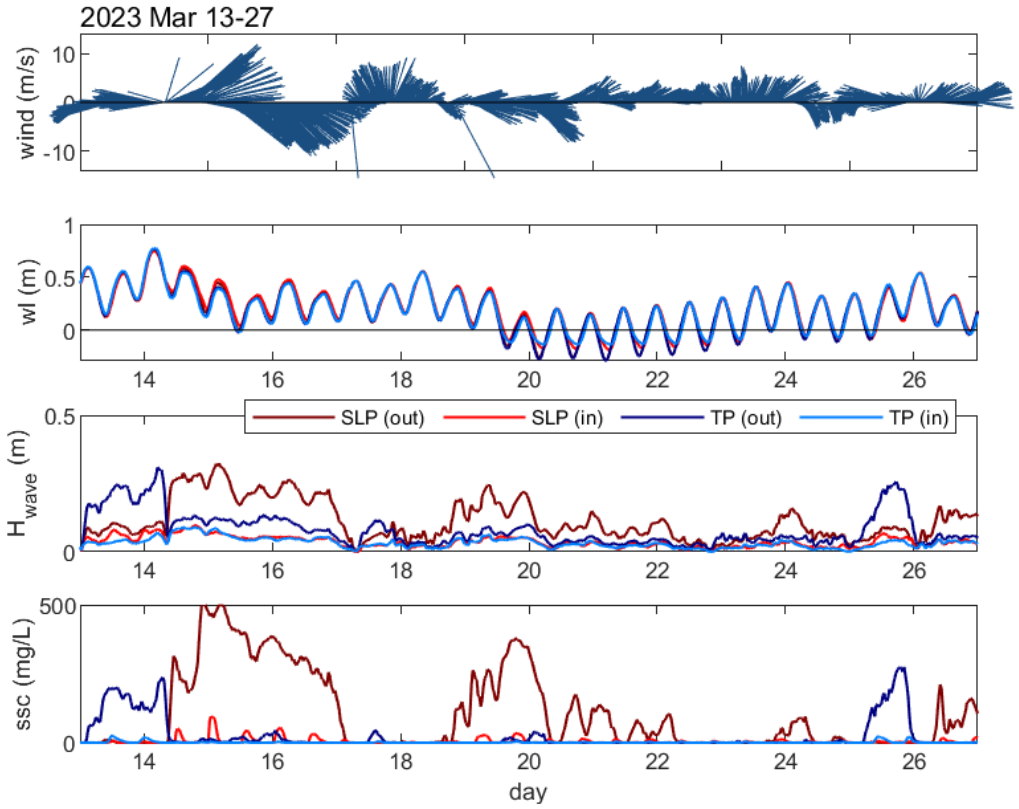

Figure 8.7. Time series from PSA scenario for March 13-27, 2023. (top) Wind vectors; (lower panels) Water level, wave height, and SSC outside and in channels to Sage Lot Pond (SLP) and Tim's Pond (TP).

An aim of the PSA simulations is to see how sediment from the placement areas gets redistributed and deposited under realistic forcing conditions. Maps of the sediment deposition for the regions around the ponds at the end of the three scenarios are shown

(Figure 8.8). While the scenarios had different forcing conditions and durations, the maps of deposition of sediment from the placements are broadly similar. Note that the sediment placement areas (outlined in blue) are net erosional. For reference the transition to salt marsh is typically found around the 0-m (MSL) elevation, and this is highlighted as a dark green bathymetric contour.

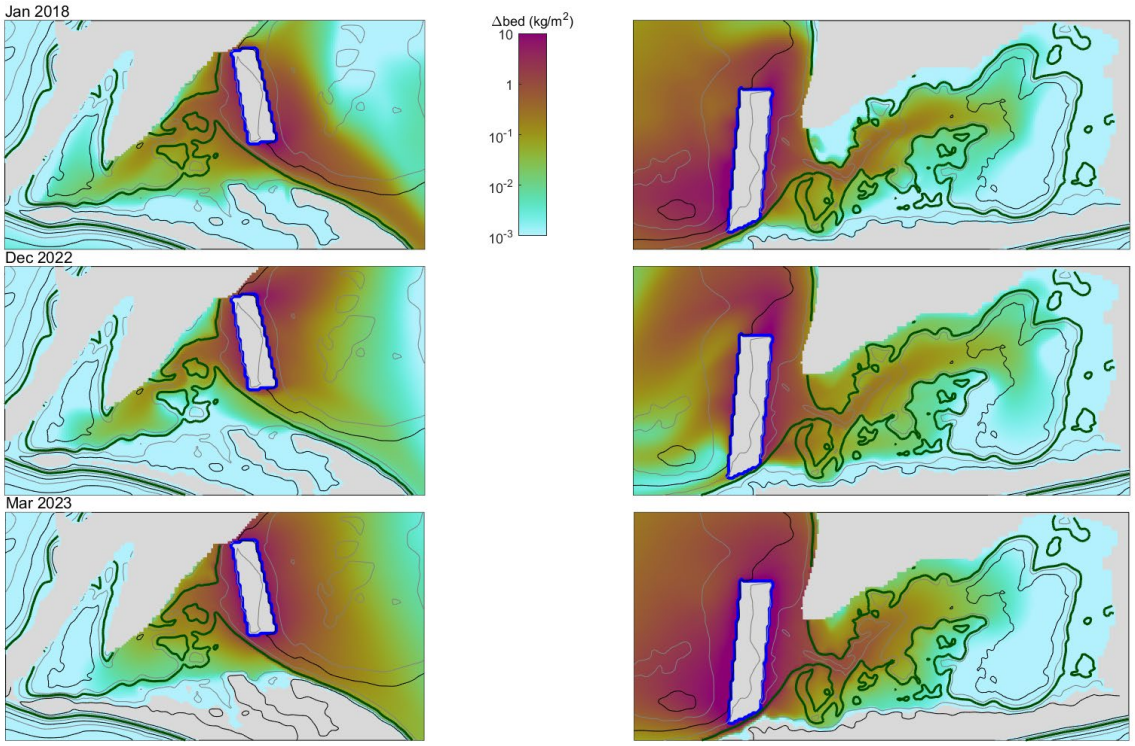

Figure 8.8 Deposited sediment mass at the end of the PSA simulations: (top) January 4-8, 2018, (middle) December 22-25, 2022, and (bottom) March 13-27, 2023.

In all the PSA scenarios, the deposited sediment mass from the placement areas decreased with distance from the source (Figure 8.8). Much of the sediment deposited in the shallow subtidal areas outside the ponds. The details of the deposition patterns depended somewhat on the forcing conditions. For example, in the January 2018 case with wind predominantly from the north, more sediment deposited along the shoreline to the south of the placement areas outside Tim's and Sage Lot Ponds, whereas for the December 2022 case with winds from the south, the deposition was more toward the north. Sediment from the PSA was also transported into the ponds and deposited in the subtidal channels and on the marshes, particularly in the regions closest to Waquoit Bay. As in the bay, the details of sediment delivery to the marsh depended on the storm conditions. For example, the northerly wind event of January 2018 resulted in greater deposition on the marshes to the south of the pond entrances than the southerly event from December 2022. The wind events and surge for the March 2023 period were not as extreme, but the sediment deposition patterns for the more moderate conditions were broadly similar to the bigger storms.

For context, the sediment mass deposition can be compared with estimates of the long-term accumulation rates for the marsh. Mineral sediment density in the Sage Lot Pond marsh is about 0.06 g/cm^3 (B. Yellen, pers. comm.). This mineral sediment density is low compared

to some marshes but is consistent with the relatively high organic fraction (0.5-0.6) of the Sage Lot marsh (Morris et al., 2016). With this sediment density and sea level rise of about 3 mm/y, the marsh must accumulate inorganic sediment at a rate of 0.02 g/cm^2/y to keep pace with sea level, or 0.2 kg/m^2. The PSA simulations were relatively short (a few days for the storm events, two weeks for the March 2023 period), but accumulation in parts of the marsh of sediment remobilized from the placement areas approach or exceed this estimate (Figure 8.8). Marsh regions farther from the pond entrance have sediment accumulation rates from the placement material that are well below the annual rate needed with SLR, but some of the sediment deposited in the entrance channels may subsequently be remobilized and deposit on marshes farther landward.

The sediment thickness for the PSA scenarios accounted for half the water depth in the placement areas, representing 0.3-0.7 m of new sediment placement (Figure 8.6). This change in depth is sufficient to alter the wave and current fields by causing shoaling of waves and increasing bottom stresses. Bed thicknesses in the placement areas decrease with erosion of sediment, the but the changes in bathymetry during the simulation periods were not incorporated into model as it ran. Instead, a maximum active bed layer thickness of 10 cm was prescribed, and if sediment mobilization exceeded this then no additional material could erode.

The changes in bed thickness at the end of the PSA simulation periods illustrate the erosion from placement areas (Figure 8.9). For the January 2018 and December 2022 storms the maximum erosion from the PSA placement was a few cm over 3-4 days of simulation. The March 2023 PSA simulation was longer (14 days) and had greater erosion – 2-4 cm outside Tim's Pond and 5-8 cm outside Sage Lot Pond. Erosion was greatest at the offshore edges of the placement areas where waves rapidly shoaled due to the sharp decrease in water depth. Net bed deposition at the end of the PSA was spread broadly but generally was small in magnitude except for near the placements. Additional analysis is needed to assess the long-term morphological evolution of PSA sediment placements. This could be informed by pilot-scale field studies in combination with modeling.

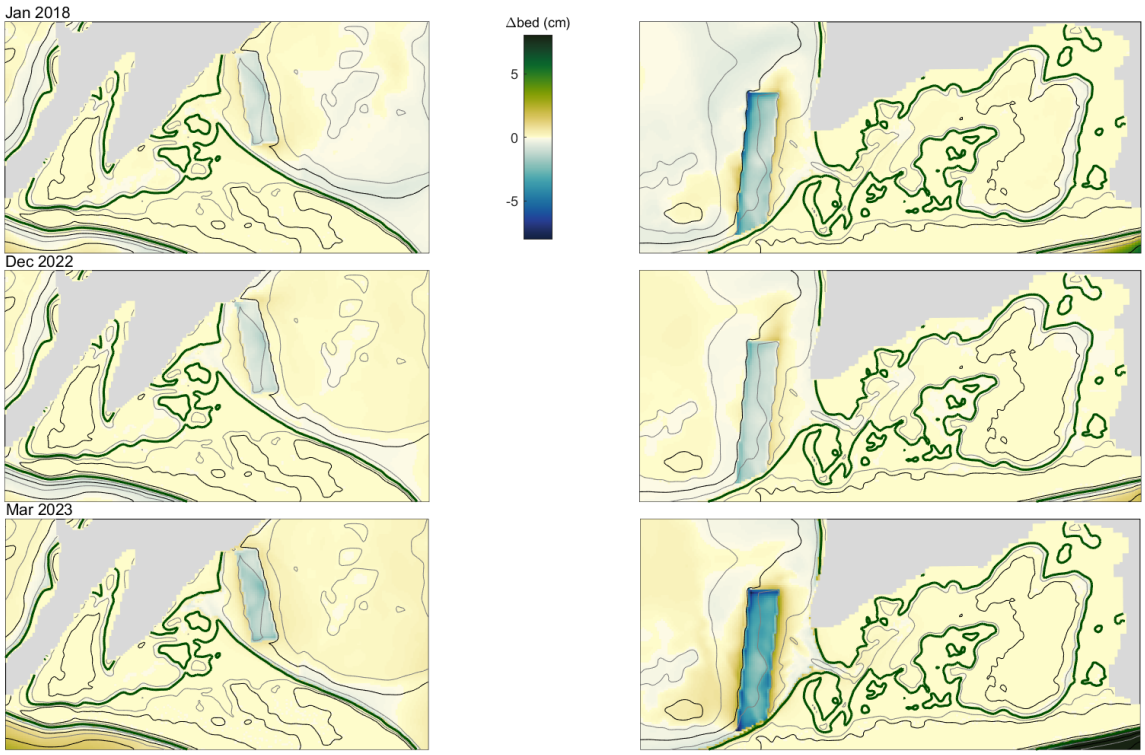

Figure 8.9 Change in bed thickness at the end of the PSA simulations: (top) January 4-8, 2018, (middle) December 22-25, 2022, and (bottom) March 13-27, 2023.

The composition of the PSA placement material consists of the three finest sediment classes in the baseline model and is meant to be representative of potential dredged material. The mobilization and transport of the placed sediment depends strongly on the particle size through the critical shear stress and settling velocity, and transport of remobilized sediment depends on sediment class. For example, in the March 2023 PSA simulation, the finest sediment class (medium silt, 0.3 mm/s setting velocity) disperses most widely and accounts for most of the sediment deposited on the marshes (Figure 8.10). In contrast, the very fine sand sediment class remains close to the placement areas and is not transported into the ponds or onto the marsh. Differences in the deposition by sediment size class were similar for the January 2018 and December 2022 storm simulations.

The full particle size distribution observed in Waquoit Bay includes sediment finer than the smallest size class modeled here, but modeling constraints limited the number of size classes. It is likely that finer sediment with lower settling velocity would be transported farther into the ponds and onto the marshes before depositing. This is consistent with observed particle size distributions from the Sage Lot Pond marsh that the median grain size was in the medium silt range. The model results indicate that using fine sediment in a PSA placement is most likely to be effective for delivering sediment to nearby marshes.

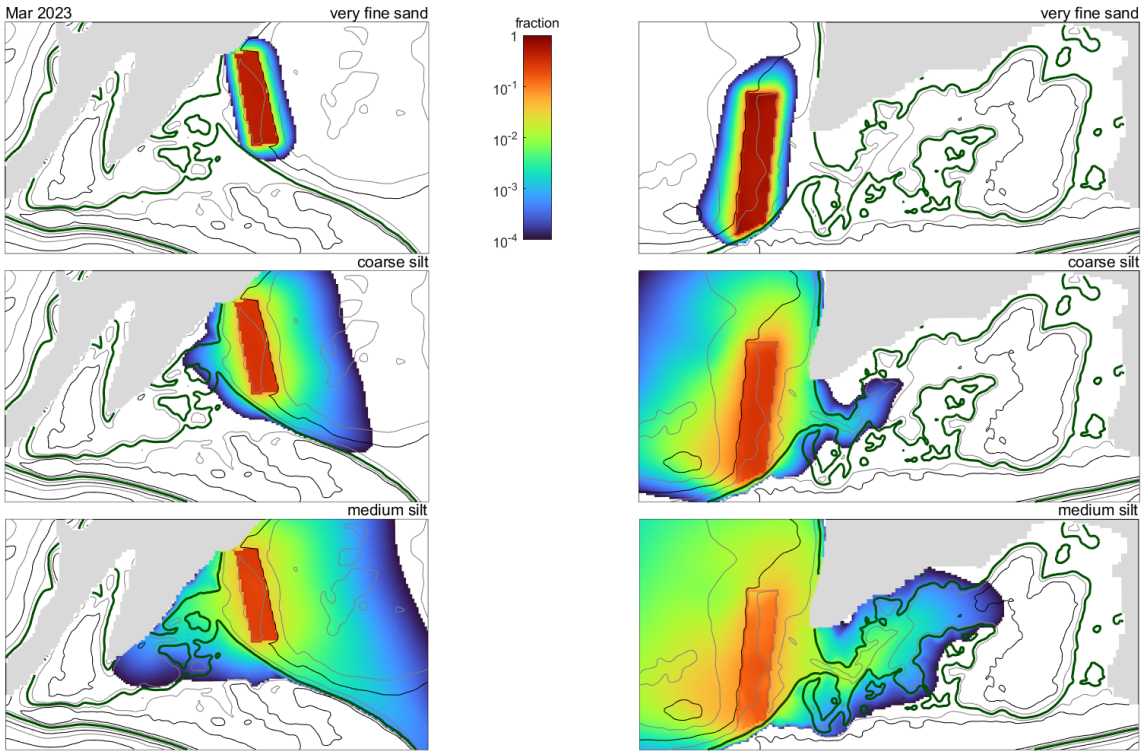

Figure 8.10 Fraction of bed sediment for different size classes at the end of the PSA simulations: (top) January 4-8, 2018, (middle) December 22-25, 2022, and (bottom) March 13-27, 2023.

To evaluate quantitatively the transport of sediment from the sediment placement areas to the ponds and surrounding marshes, the mass of sediment deposited at the end of each PSA simulation is calculated as a percentage of the initial placement mass (Table 8.2). The mass of sediment deposited on the marshes (elevation > 0 MSL) surrounding Tim's and Sage Lot Ponds are calculated, along with the total sediment deposited in the ponds plus adjacent marshes. At time scales longer than these simulations, sediment deposited in the ponds and entrance channels may eventually be remobilized and deposit more permanently on the marsh surface, and thus is relevant to the overall aims of supplying sediment to the marsh.

Table 8.2 Sediment from PSA placements depositing in ponds and on marsh

Case	Sediment	Tim's Pond		Sage Lot Pond	
		Pond + marsh	Marsh	Pond + marsh	Marsh
January 2018	Very fine sand	0.2%	0.0008%	0.006%	0.0008%
	Coarse silt	9.2%	2.1%	1.1%	0.3%
	Medium silt	17%	7.5%	4.1%	0.9%
December 2022	Very fine sand	0.6%	0.0009%	1.6%	0.6%
	Coarse silt	3.5%	0.2%	5.5%	2.2%
	Medium silt	10%	1.9%	7.6%	2.6%
March 2023	Very fine sand	0.3%	0.03%	0.2%	0.08%
	Coarse silt	7.0%	1.8%	3.0%	1.3%
	Medium silt	16%	6.7%	7.7%	3.4%

The delivery of sediment to the ponds varies by location, with the forcing conditions, and by sediment size (Table 8.2). The medium silt size class is most effectively transported from the placement area to the ponds, with 10-17% of the placement sediment going into Tim's Pond and 4-8% going into Sage Lot Pond. The fraction of the sediment depositing on the marsh at the end of the simulation was lower, with 2-8% on the marsh around Tim's Pond and 1-3% on marsh around Sage Lot. Variability among the scenarios depended on the forcing conditions. For example, the January 2018 storm with high surge during northeasterly wind was more effective at transporting sediment to Tim's Pond, whereas the December 2022 event had relatively high water levels for an extended period of southwesterly wind and was more effective at delivering sediment to Sage Lot Pond. As shown in the maps of sediment fraction by size class (Figure 8.10), the coarse silt size class was transported to the ponds and marsh at about a third to a half the rate of the medium silt. Transport of the very fine sand into the ponds was minimal (Table 8.2).

9.0 Conclusions and Considerations for Future Study

This study provides support for the feasibility of Passive Sediment Augmentation as a source of sediment nourishment within salt marshes in wave-dominated, microtidal environments such as Waquoit Bay.

The study indicates that the dominant mechanism of sediment remobilization in Waquoit Bay is wave-induced resuspension in the nearshore region, both within Waquoit Bay and in the adjacent nearshore reaches of Nantucket Sound. Wave-induced sediment resuspension predominantly occurs during storms, and the sediment is transported to marshes by tidal currents associated with storm surge, which significantly contributes to the inundation of marshes and the net delivery of sediment. Whereas the bed sediment of Waquoit Bay is a heterogeneous mixture of mud and sand, the sediment that is naturally deposited on the marshes through resuspension is mostly mud.

The same processes that result in the natural delivery of sediment to the marshes could provide the delivery of dredged sediment placed in nearshore berms proximal to the entrances of the marsh-fringed embayments. The modeling of idealized nearshore berms showed that

the finest fraction of sediment mobilized at the placement site would reach the marsh platforms during and following storm events, whereas the coarser fraction would initially remain closer to the placement sites. This resuspension and migration of the fine-grained fraction occurs over a time period of days.

The modeling study indicated that nearshore sediment berms could provide a significant augmentation of the sediment supply to the marshes, potentially increasing the sediment supply by a factor of 2 or more over the natural rate. However, the field and modeling study were not adequate to obtain a firm quantification of that rate. The uncertainties related to the modeling analysis are discussed below.

This study suggests that Passive Sediment Augmentation may be a plausible candidate for beneficial use of dredged sediment. In Waquoit Bay and similar environments, the predominantly fine-grained sediment that could be obtained from a local dredging projects would be appropriate for the placement of PSA berms. The same sediment that is transported to the marsh platform by natural processes would be supplied by the PSA placement material, albeit with augmented concentrations due to the proximity of the mounds and their enhanced erodibility. The modeling suggests that the benthic conditions of the Bay would not be significantly altered by the PSA emplacements, based on estimation of changes of bed thickness on the order of millimeters outside the immediate vicinities of the placements.

This study did not answer all of the questions related to Passive Sediment Augmentation. There remain some issues that would need to be addressed in context with implementation in microtidal environments such as Waquoit Bay, and the study does not address the different dynamical regimes of the mesotidal marshes that are found elsewhere along the coast of Massachusetts.

One important issue that could not be determined without additional study is the actual rate of sediment remobilization associated with PSA placements. This rate determines the quantity of sediment delivered to the marshes as well as the timescale for the immediate environment around the PSA berms to return to background benthic conditions. The most effective way of addressing this issue would be to perform pilot experiments with small mounds or berms of sediment with the appropriate grain-size distribution, using some sediment-associated tracer and repeated surveys to keep track of the diminution of the placement, as well as the pathways of transport of the remobilized sediment.

Another limitation of this study is that the natural processes responsible for the transport of sediment to the marshes are not adequately quantified. This study clearly identified the dominant processes, but the rates are still uncertain due to inadequate quantification of sediment resuspension and transport at a systemwide scale, from Nantucket Sound, through Waquoit Bay and extending across the marsh platforms themselves. At event to seasonal time scales, transport of sediment into the ponds and onto the marshes comes primarily from local resuspension by waves of fine sediment in the shallow regions offshore of the ponds. At longer time scales, the system is generally accumulating sediment at rates consistent with sea level rise (Maio et al. 2016). Since Waquoit Bay does not have substantial sediment inputs from the uplands (e.g., river discharge, shoreline erosion), much of the sediment depositing in the bay must be coming from offshore in Nantucket Sound. However, the data needed to determine where the sediment supplying the bay is sourced or the processes bring it into the system are lacking. Additionally, sediment deposited in the ponds during storm events likely contributes to the accumulation of sediment on the marsh at longer time scales, but the mechanisms behind this require further observations. Evidence indicates that unlike

the deeper parts of the bay, the marsh is not keeping up with sea level rise, as seen in deposition rates from sediment elevation tables less of than 3 mm/y, erosion of creek banks due to burrowing crabs and conversion of vegetated platform to open water extent. PSA could help augment the delivery of fine sediment to the marsh and help mitigate the threat from sea level rise. To evaluate the relative benefits of the PSA approach, the rate of delivery of sediment it accomplishes must be considered in context with measured rates of sediment transport and accumulation via natural processes, which require further investigation.

Waquoit Bay is representative of wave-dominated microtidal estuarine and salt marsh systems in Massachusetts. However, other areas of the state consist of mesotidal salt marsh systems. Consideration of PSA in mesotidal environments, such as the marshes in embayments along the South Shore, North Shore, and Cape Cod Bay, would require a separate study of a similar scope to this study. The mechanisms of sediment mobilization in mesotidal environments are likely to be more strongly influenced by tidal currents, and the transport to marshes is likewise more strongly associated with tidal conditions than the wave-dominated regime of Waquoit Bay. In addition to consideration of tides, the sources of sediment that potentially supply the marsh environment vary from system to system. Much of the coast of Massachusetts has sediment supplied from coastal erosion of glacial till and outwash deposits, but in the vicinity of significant riverine inflow (e.g., the Merrimack River), fluvial sediment sources are also important.

10.0 References

Aubrey, D. G., McSherry, T. R., & Eliet, P. P. (1993). Effects of multiple inlet morphology on tidal exchange: Waquoit Bay, Massachusetts. *Formation and Evolution of Multiple Tidal Inlets*, *44*, 213-235.

Booij, N., Ris, R.C., Holthuijsen, L.H., 1999. A third-generation wave model for coastal regions 1. Model description and validation. Journal of Geophysical Research 104, PP. 7649-7666, doi:199910.1029/98JC02622.

Crawford, R. E. (2002). Secondary wake turbidity from small boat operation in a shallow sandy bay. *Journal of Coastal Research*, 50-65.

Haidvogel, D.B., Arango, H., Budgell, W.P., Cornuelle, B.D., Curchitser, E., Di Lorenzo, E., Fennel, K., Geyer, W.R., Hermann, A.J., Lanerolle, L., Levin, J., McWilliams, J.C., Miller, A.J., Moore, A.M., Powell, T.M., Shchepetkin, A.F., Sherwood, C.R., Signell, R.P., Warner, J.C., Wilkin, J., 2008. Ocean forecasting in terrain-following coordinates: Formulation and skill assessment of the Regional Ocean Modeling System. Journal of Computational Physics 227, 3595–3624, doi:10.1016/j.jcp.2007.06.016.

Larson, J., Jacob, R., Ong, E., 2005. The model coupling toolkit: a new Fortran90 toolkit for building multiphysics parallel coupled models. International Journal of High Performance Computing Applications 19, 277–292.

Maio, C. V., Donnelly, J. P., Sullivan, R., Madsen, S. M., Weidman, C. R., Gontz, A. M., & Sheremet, V. A. (2016). Sediment dynamics and hydrographic conditions during storm passage, Waquoit Bay, Massachusetts. *Marine Geology*, *381*, 67-86.

Maio, C. V., Gontz, A. M., Weidman, C. R., & Donnelly, J. P. (2014). Late Holocene marine transgression and the drowning of a coastal forest: Lessons from the past, Cape Cod, Massachusetts, USA. *Palaeogeography, Palaeoclimatology, Palaeoecology*, *393*, 146-158.

Morris, J.T., Barber, D.C., Callaway, J.C., Chambers, R., Hagen, S.C., Hopkinson, C.S., Johnson, B.J., Megonigal, P., Neubauer, S.C., Troxler, T., Wigand, C., 2016. Contributions of organic and inorganic matter to sediment volume and accretion in tidal wetlands at steady state. Earth's Future 4, 110–121, doi:10.1002/2015EF000334.

Orson, R. A., & Howes, B. L. (1992). Salt marsh development studies at Waquoit Bay, Massachusetts: Influence of geomorphology on long-term plant community structure. *Estuarine, Coastal and Shelf Science*, *35*(5), 453-471.

Shchepetkin, A.F., McWilliams, J.C., 2005. The regional oceanic modeling system (ROMS): a split-explicit, free-surface, topography-following-coordinate oceanic model. Ocean Modelling 9, 347–404, doi:10.1016/j.ocemod.2004.08.002.

Warner, J.C., Armstrong, B., He, R., Zambon, J.B., 2010. Development of a Coupled Ocean–Atmosphere–Wave–Sediment Transport (COAWST) Modeling System. Ocean Modelling 35, 230–244, doi:10.1016/j.ocemod.2010.07.010.

Warner, J.C., Sherwood, C.R., Signell, R.P., Harris, C.K., Arango, H.G., 2008. Development of a three-dimensional, regional, coupled wave, current, and sediment-transport model. Computers & Geosciences 34, 1284–1306, doi:10.1016/j.cageo.2008.02.012.

Appendix A: Results of Grain Size analysis of Grab Samples

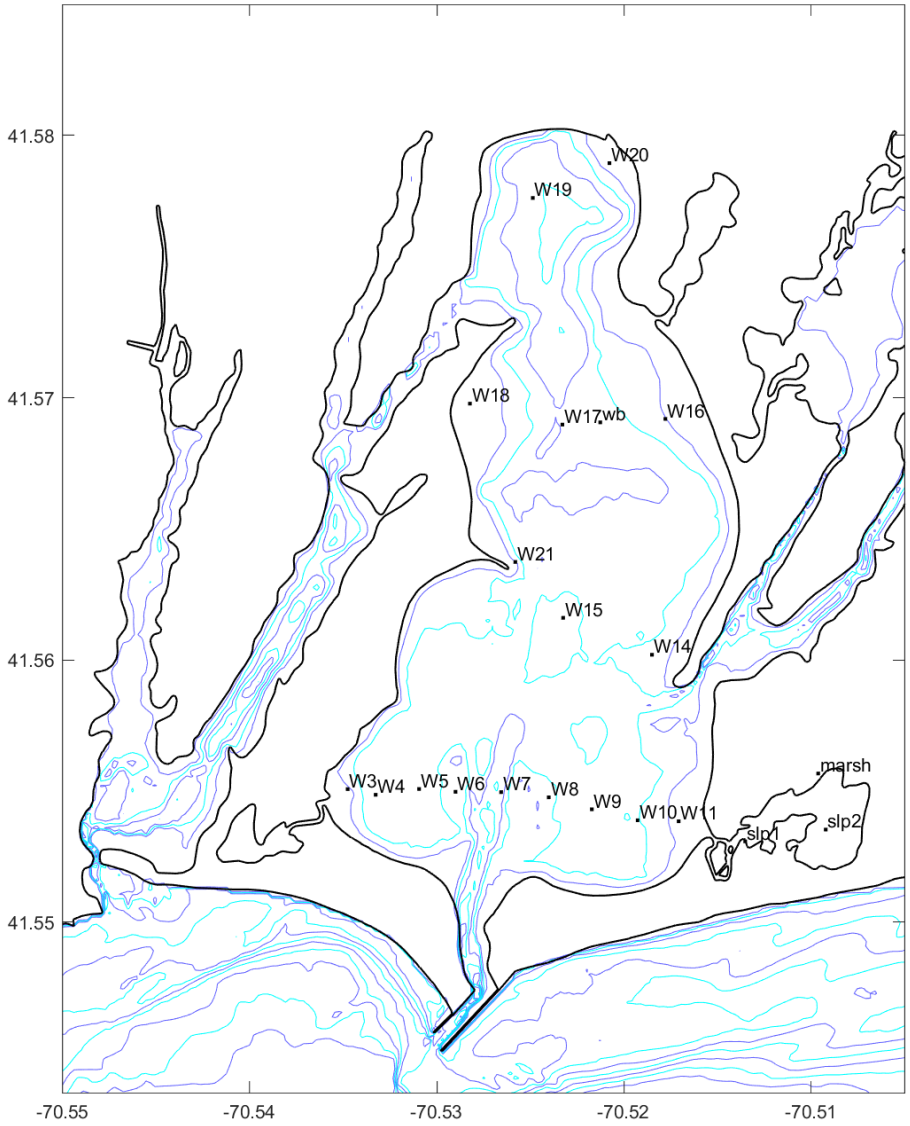

Figure A.1 Locations of grab samples, obtained on May 3, 2023.

Table A.1: Results of Grain Size Analysis

Fine fraction: percent smaller than 63 μm. D50: 50th percentile (median) diameter.
Bulk density: dry density. LOI: Loss on Ignition.

Station	latitude	longitude	depth	sediment type	fine fraction	D50	Bulk Density	LOI
			m		%	μm	g/cm³	%
W3	41 33.304	70 32.086	0.9	very coarse sand	24	666	1.41	0
W4	41 33.291	70 31.996	1.8	coarse silt	57	46	0.72	6
W5	41 33.305	70 31.858	2.1	very fine sand	51	59	0.95	4
W6	41 33.299	70 31.741	1.5	very fine sand	40	76	1.52	1
W7	41 33.298	70 31.594	2.4	very fine sand	45	76	0.64	5
W8	41 33.286	70 31.441	1.8	very fine sand	51	59	1.68	1
W9	41 33.258	70 31.303	1.8	coarse silt	52	52	0.82	7
W10	41 33.233	70 31.156	1.8	coarse silt	60	46	1.48	2
W11	41 33.231	70 31.024	0.9	coarse sand	10	634	1.74	0
W14	41 33.612	70 31.110	1.5	medium sand	14	352	1.86	1
W15	41 33.696	70 31.395	1.5	coarse silt	57	46	0.38	15
W16	41 34.151	70 31.067	1.2	coarse sand	14	516	1.62	0
W17	41 34.138	70 31.398	2.7	very fine sand	39	86	0.28	20
W18	41 34.187	70 31.694	1.8	medium sand	41	86	1.22	2
W19	41 34.657	70 31.493	2.4	coarse silt	62	40	0.37	15
W20	41 34.736	70 31.247	2.4	coarse silt	58	46	0.46	13
W21	41 33.824	70 31.549	1.2	coarse sand	15	400	2.03	0
slp2	41 33.212	70 30.553	1.2	fine sand	34	111	0.39	14
marsh	41 33.340	70 30.577	0.0	very fine sand	41	86	0.24	43
slp1	41 33.185	70 30.811	0.3	coarse sand	9	586	1.82	0
wb	41 34.143	70 31.276	2.1	medium sand	38	111	0.24	23

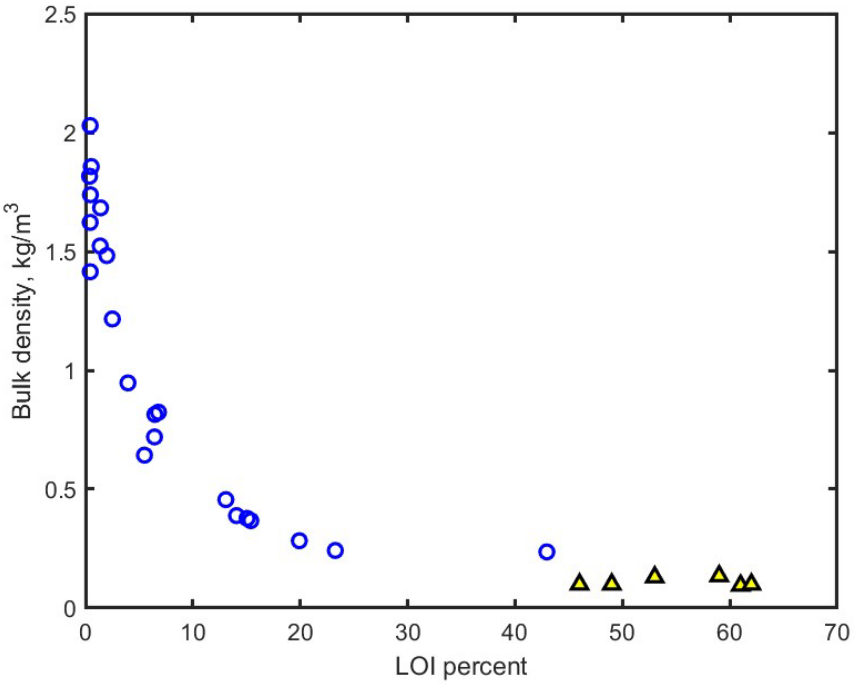

Figure A.2 Relationship between LOI and bulk density for the grab samples (blue circles) as well as samples from the Sage Lot Pond marsh (Brian Yellen, unpublished results).

Appendix B: Calibration of the Suspended Sediment

The original plan for quantifying suspended sediment concentration was to use the optical backscatter sensors. The sensors were calibrated in the lab by measuring the signal of the instruments in a bucket with several known concentrations of suspended sediment. The suspensions were generated by using a measured volume of sediment from station W9 (coarse silt), which was deemed to be representative of the fine sediment resuspension in the vicinity of the measurement sites. The results of this calibration are shown in Figure B.1.

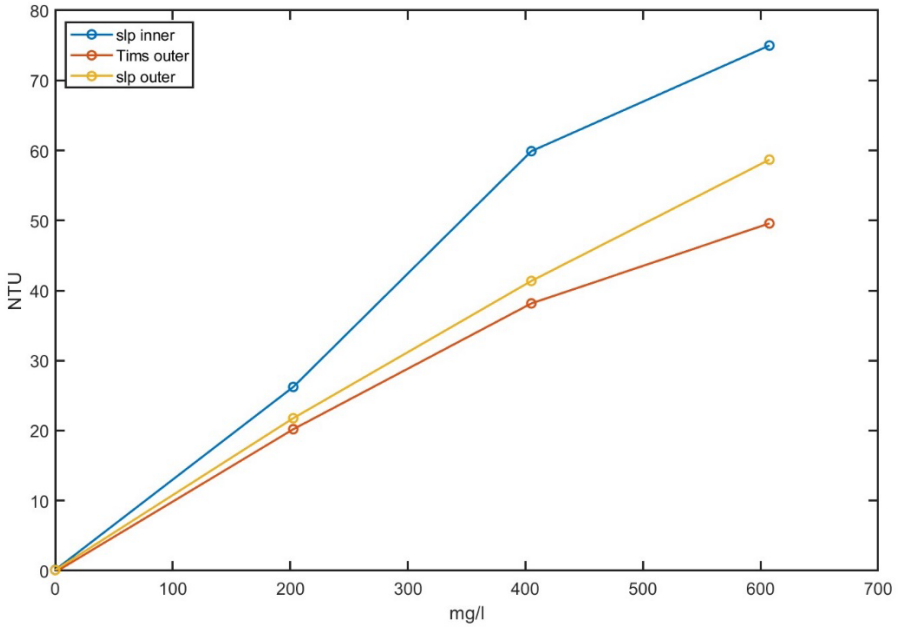

Figure B.1 Calibration of 3 OBS sensors based on suspended sediment samples from station W9. The x-axis is the concentration of the suspended sediment, and the y-axis is the output of three of the four OBS sensors, in NTUs. The 4th sensor malfunctioned during the calibration.

This calibration indicated surprisingly high concentrations for a given output of the sensors, in that optical backscatter calibrations from other estuarine environments typically give conversion factors between NTU and mg/l of around 1. The difference is explained by the presence of a significant sand fraction in the samples (see Table A.1). Sand produces a weak OBS response, whereas it contributes a significant fraction of the mass of sediment that determines its concentration. During the lab calibration, the sample was vigorously stirred during the measurement, resulting in a uniform concentration of the sand-silt mixture. This is likely to be different from the field situation, in which the vertical distribution of sand has a significant vertical gradient due to its rapid settling velocity. We corrected for this mismatch between the lab and field distributions by reducing the calibration factor by a factor of 2, which we felt would provide a more representative estimate of the concentration 0.4 m above the bed.

Unfortunately, these sensors all became seriously fouled following the deployment, probably as a result of marsh detritus that interfered with the optical signal. One of the sensors, located at the Outer Tim's Pond site, had a long enough period of noisy but

serviceable data to provide a cross-calibration with the acoustic backscatter signal from the Aquadopp at the same location. Figure B.2 shows the timeseries of the two sensors over the period in which the OBS data showed a signal that could be interpreted.

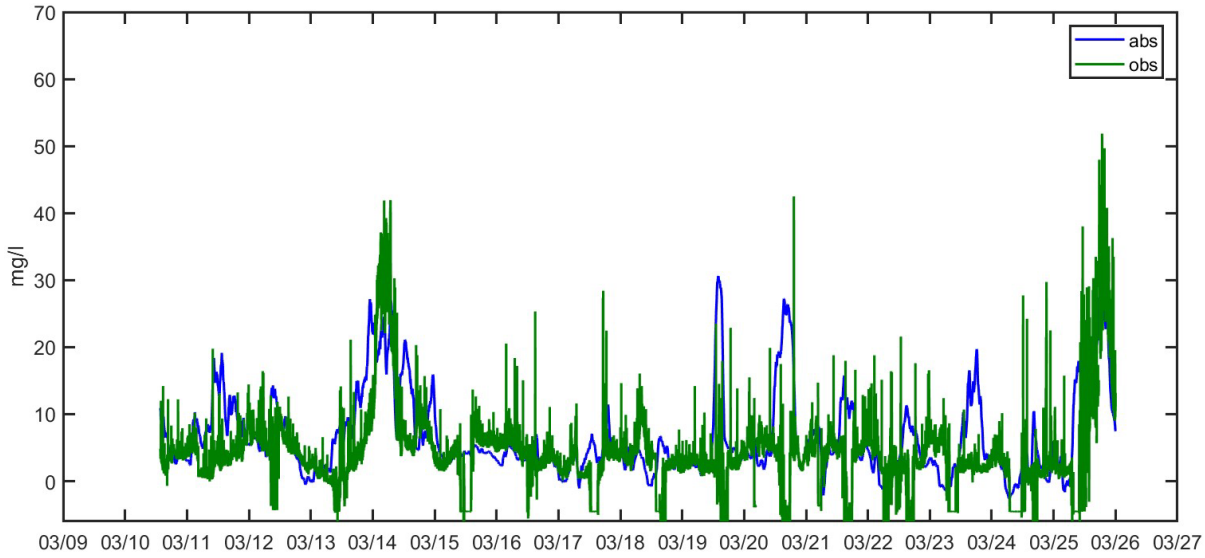

Figure B.2 Comparison of the acoustic backscatter signal (abs) from the Aquadopp to the optical backscatter (OBS) at the Tim's Pond Outer station for the period over which the OBS signal could be interpreted.

The equation used to convert the abs signal to concentration was empirically determined to match the peaks and troughs of the OBS signal, ignoring the negative pulses of the OBS, which were deemed to be artifacts associated with fouling of the sensor.

$$Concentration = 14(exp(abs/110)-12)$$

Appendix C: Calculation of Significant Wave Height

Pressure measurements were obtained by Lowell strain-gauge sensors, sampling at 4 Hz. These instruments were placed at a fixed height, 0.4 m above the bottom, roughly 0.4 m below mean low water. The height of the water surface above the sensors varied from 0 to 1.4 m above the sensors.

The significant wave height is defined as 4 times the standard deviation of the wave-induced fluctuations of surface elevation. To remove low-frequency variations in water level not due to surface waves, the pressure data were filtered to remove all fluctuations with periods longer than 9 seconds. Analysis for wave variables was conducted for 1-minute intervals of the 4 Hz data. The dominant period (T) was determined by counting the zero-crossings (n_{zero}) of the filtered data for each 1-minute window, with $T = 60 \times 2 / n_{zero}$.

Once the period was determined, the attenuation of the pressure signal between the water surface and the depth of the measurement had to be determined. This was accomplished by using linear shallow-water wave theory. First, linear wave theory was used to determine the wave-number of the dominant wave based on its period and the water depth at the time of the measurement. Then the amount of attenuation of the wave was determined from the position of the sensor in the water column, based on the attenuation of the signal with depth according to the formula

$$p = \rho\, g\, a\, \cosh(k z) / \cosh(k h)$$

where p is the pressure, ρ is the water density, g is the acceleration of gravity, a is the amplitude of the wave, cosh is the hyperbolic cosine, k is the wavenumber, z is the height of the sensor above the bottom, and h is the total water depth. When the sensor was close to the water surface, the attenuation factor cosh (k z) / cosh (k h) was only slightly less than 1, but when the water level was high and/or the waves were very short, the attenuation factor fell to values below 0.1, indicating little wave signal reaching the pressure sensor. When that value fell below 0.1, the estimate of significant wave height was discarded. The blank spots in the significant wave height record in Figures 5.6 and 5.7 correspond to these conditions. This mainly occurred when the wave forcing was weak at a particular location, leading to short waves.